AD-A167 119 NUMERICAL SIMULATION OF THE LASER-TARGET INTERACTION AND BLAST WAVE FORMA..(U) NAVAL RESEARCH LAB WASHINGTON DC J L GIULIANI ET AL. 09 MAY 86 NRL-MR-5762 1/1

UNCLASSIFIED F/G 20/5 NL

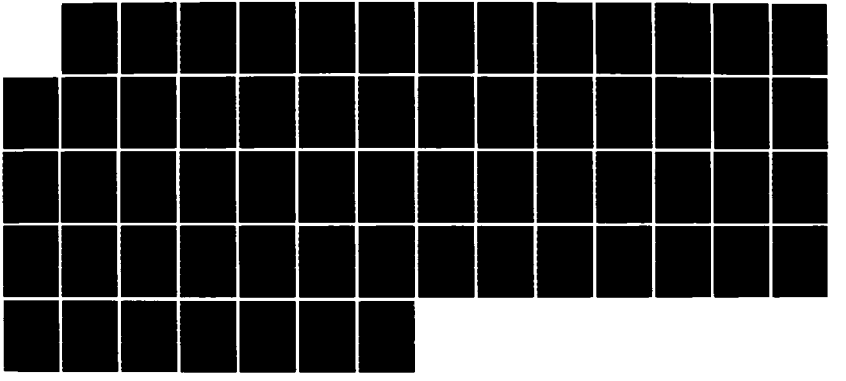

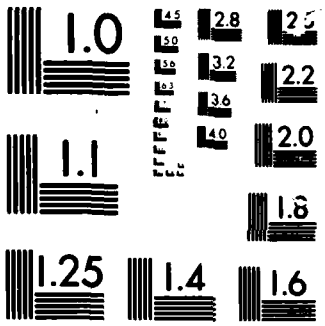

NRL Memorandum Report 5762

Numerical Simulation of the Laser-Target Interaction and Blast Wave Formation in the DNA/NRL Laser Experiment

JOHN L. GIULIANI, JR. AND MARGARET MULBRANDON

Geophysical and Plasma Dynamics Branch
Plasma Physics Division

May 9, 1986

This research was sponsored by the Defense Nuclear Agency under Subtask W99QMXWA, work unit 00010 and work unit title "Plasma Structure Evolution."

NAVAL RESEARCH LABORATORY
Washington, D.C.

DISCLAIMER NOTICE

THIS DOCUMENT IS BEST QUALITY PRACTICABLE. THE COPY FURNISHED TO DTIC CONTAINED A SIGNIFICANT NUMBER OF PAGES WHICH DO NOT REPRODUCE LEGIBLY.

AD-A167119

SECURITY CLASSIFICATION OF THIS PAGE

REPORT DOCUMENTATION PAGE

1a. REPORT SECURITY CLASSIFICATION UNCLASSIFIED	1b. RESTRICTIVE MARKINGS
2a. SECURITY CLASSIFICATION AUTHORITY	3. DISTRIBUTION / AVAILABILITY OF REPORT Approved for public release; distribution unlimited.
2b. DECLASSIFICATION / DOWNGRADING SCHEDULE	
4. PERFORMING ORGANIZATION REPORT NUMBER(S) NRL Memorandum Report 5762	5. MONITORING ORGANIZATION REPORT NUMBER(S)
6a. NAME OF PERFORMING ORGANIZATION Naval Research Laboratory 6b. OFFICE SYMBOL (If applicable) Code 4780	7a. NAME OF MONITORING ORGANIZATION
6c. ADDRESS (City, State, and ZIP Code) Washington, DC 20375-5000	7b. ADDRESS (City, State, and ZIP Code)
8a. NAME OF FUNDING / SPONSORING ORGANIZATION Defense Nuclear Agency 8b. OFFICE SYMBOL (If applicable) RAAE	9. PROCUREMENT INSTRUMENT IDENTIFICATION NUMBER
8c. ADDRESS (City, State, and ZIP Code) Washington, DC 20305	10. SOURCE OF FUNDING NUMBERS PROGRAM ELEMENT NO: 63223C; PROJECT NO:; TASK NO.:; WORK UNIT ACCESSION NO: BR010-43

11. TITLE (Include Security Classification) Numerical Simulation of the Laser-Target Interaction and Blast Wave Formation in the DNA/NRL Laser Experiment

12. PERSONAL AUTHOR(S)
Guiliani, John L., Jr. and Mulbrandon, Margaret

13a. TYPE OF REPORT	13b. TIME COVERED	14. DATE OF REPORT (Year, Month, Day)	15. PAGE COUNT
Interim	FROM _____ TO _____	1986 May 9	60

16. SUPPLEMENTARY NOTATION
This research was sponsored by the Defense Nuclear Agency under Subtask W99QMXWA, work unit 00010 and work unit title "Plasma Structure Evolution."

17. COSATI CODES		
FIELD	GROUP	SUB-GROUP

18. SUBJECT TERMS (Continue on reverse if necessary and identify by block number)
Laser plasmas, Numerical simulation
Blast wave, Raleigh-Taylor instability

19. ABSTRACT (Continue on reverse if necessary and identify by block number)

A numerical simulation of the ablation of a planar, aluminum foil target by a neodymium laser in the presence of a 2.5 Torr nitrogen background gas is presented. The simulation includes inverse bremsstrahlung absorption during the laser pulse, the cold isotherm in the equation of state for solid aluminum, non-equilibrium chemistry for both the target material and the background gas, radiation transport of the continuum, ion and electron energy equations, and blast wave formation in the background gas. The simulation is followed out to > 50 nsec from the peak of the laser pulse. Although the Lagrangian code is 1-D, the divergence of the ablated target material expanding toward the laser (forward) as well as the rearward acceleration of the remaining target is accounted for by using an oblate spheroidal coordinate system.

The primary results of the simulations are as follows: (i), by ~ 50 nsec a cavity with $T_e \sim 60$ ev and $n_e \sim 2\times10^{+17}$ cm^{-3} has formed behind the denser and cooler forward moving blast wave; (ii), this cavity is not in chemical equilibrium but highly overionized for its temperature with predominantly Al^{+9}, Al^{+10}, Al^{+11}, N^{+5} and N^{+6}; and (iii), the conditions for a deceleration driven Rayleigh-Taylor instability are satisfied at the rear blast wave near one equal mass radius. This last feature may account for the experimentally observed floculli on the rearward side.

20. DISTRIBUTION / AVAILABILITY OF ABSTRACT	21. ABSTRACT SECURITY CLASSIFICATION
☒ UNCLASSIFIED/UNLIMITED ☐ SAME AS RPT. ☐ DTIC USERS	UNCLASSIFIED
22a. NAME OF RESPONSIBLE INDIVIDUAL J. D. Huba	22b. TELEPHONE (Include Area Code) (202) 767-3630 22c. OFFICE SYMBOL Code 4780

DD FORM 1473, 84 MAR 83 APR edition may be used until exhausted
All other editions are obsolete

SECURITY CLASSIFICATION OF THIS PAGE

CONTENTS

NUMERICAL SIMULATION OF THE LASER-TARGET INTERACTION AND BLAST WAVE FORMATION IN THE DNA/NRL LASER EXPERIMENT

I. INTRODUCTION

Over the past several years the Plasma Physics Division at the Naval Reasearch Laboratory has developed an experimental apparatus which is intended to simulate certain physical processes characteristic of a high altitude nuclear explosion (HANE)[1]. This program is under the auspices of the Division of Atmospheric Effects of the Defense Nuclear Agency. It has the primary goal of a physical understanding and reliable prediction of the degradation of radar and communication systems through a HANE-disturbed environment.

The first series of experiments (ending March 1985) were initiated by irradiating one side of a thin foil target with a neodymium laser. Dark-field shadowgraphy for the case of a high pressure (> 1 Torr) ambient gas taken at 50 to 150 nsec after the laser pulse show that the rapid heating and evaporation of the target material is followed by a blast wave expanding toward the laser[2,3], here denoted as the forward direction. Except for the pronounced aneurism, which is found at high pressures (~5 Torr) and generally occurs near the laser axis, the blast wave appears quite smooth. On the other hand for those targets supported by a stalk, shadowgraphy reveals that the rearward moving blast wave is very disrupted with many small flocculi. The forward aneurism and rearward flocculi are relevant to the question of whether structure can be seeded in the early stages of blast wave

Manuscript approved January 29, 1986.

formation. To understand the mechanisms responsible for these observed features it is clearly necessary to have a realistic model for the initial laser-target interaction and the subsequent formation of the blast wave. This report presents the results of a numerical simulation of these different stages. The code includes a number of pertinent physical processes in order to provide a complete qualitative picture of the dynamics. Existing measured data on the electron number density and spectroscopy can be used for quantitative verification of the numerical simulation. Since the code is one dimensional it cannot directly answer the question of early time stucture, but it is a step toward a global model for the DNA/NRL laser experiment and, as such, can be used as a framework for more detailed studies.

The results from the numerical models show a hot (T_e -30-70 ev), dense (n_e -few x10^{+17} cm^{-3}) cavity pushing on the forward moving blast wave after -50 nsec. At this time the engulfed ambient mass is much larger than the amount of ablated material. The gross structure of this forward half of the blowoff is similar to an isothermal, Taylor-Sedov blast wave and the outflow within the cavity is subsonic. This cavity however, is filled with Al^{+9}, Al^{+10}, Al^{+11}, N^{+5}, and N^{+6}, indicating a highly non-equilibrium plasma. On the rear side, the blast wave is colder and denser and it is found to satisfy a Rayleigh-Taylor instability criterion at - 40 nsec. This is roughly the time when the rearward accelerated debris has swept-up an equivalent target mass. The overall results further suggest that the radiating line cores should be optically thick.

In the next section we discuss the code in detail by enumerating the physical processes included in it. In section III we describe a standard run and make comparisons with other runs which employ ad hoc assumptions for chemistry and radiative line transfer. In the final section we summarize our main conclusions and make comparisons with the experiment. The limitations of the present code are also presented here.

II. DISCUSSION OF THE SIMULATION

A. Hydrodynamics.

The basic hydrodynamic equations to be solved are the continuity equation,

$$\frac{\partial \rho}{\partial t} + \nabla \cdot \rho \mathbf{v} = 0, \tag{1}$$

the total momentum equation,

$$\rho \frac{\partial \mathbf{v}}{\partial t} + \rho \mathbf{v} \nabla \cdot \mathbf{v} + \nabla (p_i + p_e) + \nabla : \mathbf{Q}_{vis} = 0, \tag{2}$$

the ion internal energy equation,

$$\frac{\partial}{\partial t}(\rho \varepsilon_i) + \nabla \cdot \mathbf{v} \rho \varepsilon_i + p_i \nabla \cdot \mathbf{v} + (\mathbf{Q}_{vis} : \nabla)\mathbf{v} + \nabla \cdot \mathbf{q}_i = Q_{ie} \tag{3}$$

and the electron internal energy equation,

$$\frac{\partial}{\partial t}(\rho_e \varepsilon_e) + \nabla \cdot \mathbf{v} \rho_e \varepsilon_e + p_e \nabla \cdot \mathbf{v} + \nabla \cdot \mathbf{q}_e = -Q_{ie} + \Lambda + H_L. \tag{4}$$

Here ρ is the total mass density, ρ_e is the electron mass density, $\mathbf{v}$ is the mass velocity, p_i and p_e are the ion and electron pressure, $\mathbf{q}_i$ and $\mathbf{q}_e$ are the ion and electron thermal conduction, ε_i and ε_e are the ion and electron specific internal energies, Λ is the electron energy change due to radiation and ionization, and H_L is the electron heating due to absorption of the laser energy to be described below (eqn.[30]). Q_{ie} is the thermal equilibration term from Braginskii[4]

$$Q_{ie} = 3 \frac{\rho_e}{m_i \tau_e} k_B (T_e - T_i), \tag{5}$$

where m_i is the mean ion mass and τ_e is the electron collision time. Q_{vis} is a tensor artificial viscosity added to smooth out shocks and it has the form suggested by Noh[5] including an artificial heat flux near shocks. A tensor product involving the artificial viscosity is denoted by a colon. We have also assumed that there are no currents so that the ion and electron velocities are equal.

We will limit our analysis so that the variables depend on time and only one spatial coordinate in a general orthogonal coordinate system. Let this coordinate be ξ_1 and the scale factors be h_1, h_2, and h_3. Then with $\mathbf{v} = ve_1$, $\mathbf{q} = qe_1$, and $\mathbf{Q} = Qe_1e_1$ one finds for the continuity, momentum, and internal energy equations,

$$\frac{\partial \rho}{\partial t} + \frac{1}{h_1h_2h_3}\frac{\partial}{\partial \xi_1}(h_1h_2h_3\rho v) = 0, \tag{6}$$

$$\frac{\partial \rho v}{\partial t} + \frac{1}{h_1h_2h_3}\frac{\partial}{\partial \xi_1}(h_2h_2\rho v^2 + Q_{vis}) + \frac{1}{h_1}\frac{\partial}{\partial \xi_1}(p_i + p_e) = 0, \tag{7}$$

$$\frac{\partial}{\partial t}(\rho\varepsilon_i) + \frac{1}{h_1h_2h_3}\frac{\partial}{\partial \xi_1}[h_2h_3(\rho\varepsilon_i v + q_i)] + \frac{p_i}{h_1h_2h_3}\frac{\partial}{\partial \xi_1}(h_2h_3v) + Q_{vis}\frac{1}{h_1}\frac{\partial v}{\partial \xi_1} = Q_{ie}, \tag{8}$$

and,

$$\frac{\partial}{\partial t}(\rho_e\varepsilon_e) + \frac{1}{h_1h_2h_3}\frac{\partial}{\partial \xi_1}[h_2h_3(\rho_e\varepsilon_e v + q_e)] + \frac{p_e}{h_1h_2h_3}\frac{\partial}{\partial \xi_1}(h_2h_3v) = -Q_{ie} + \Lambda + H_L. \tag{9}$$

Let us define the area as

$$A(\xi_1) = \iint h_2h_3 d\xi_2 d\xi_3 \tag{10}$$

where the integration limits extend over the allowed range in ξ_2 and ξ_3. Now note that for an arbitrary function $X(\xi_1)$,

$$\iiint \frac{\partial X}{\partial t}\, dVol = \iiint \frac{\partial X}{\partial t}\, h_1 h_2 h_3 d\xi_1 d\xi_2 d\xi_3 = \int \frac{\partial X}{\partial t}\, A h_1 d\xi_1,$$

$$= \frac{D}{Dt} \int XAh_1 d\xi_1 - (AXv)\Big|_{\xi_1 = a}^{\xi_1 = b},$$

where the range of integration over ξ_1 is a to b and D/Dt is the time derivative following the fluid. Integrating each equation (6)-(10) over a volume element and using the above relation gives

$$\frac{D}{Dt} \int_b^a \rho A h_1 d\xi_1 = 0, \tag{11}$$

$$\frac{D}{Dt} \int_a^b (\rho v A h_1) d\xi_1 + \int_a^b A \frac{\partial (p_i + p_e)}{\partial \xi_1}\, d\xi_1 + (AQ_{vis})\Big|_a^b = 0, \tag{12}$$

$$\frac{D}{Dt} \int_a^b (\rho \varepsilon_i A h_1) d\xi_1 + \int_a^b p_i \frac{\partial (Av)}{\partial \xi_1}\, d\xi_1 + (Aq_i)\Big|_a^b$$

$$+ \int_a^b AQ_{vis} \frac{\partial v}{\partial \xi_1}\, d\xi_1 = \int_a^b Q_{ie} A h_1 d\xi_1, \tag{13}$$

and,

$$\frac{D}{Dt} \int_a^b (\rho_e \varepsilon_e A h_1)\, d\xi_1 + \int_a^b p_e \frac{\partial (Av)}{\partial \xi_1}\, d\xi_1 + (Aq_e)\Big|_a^b$$

$$= \int_a^b (-Q_{ie} + \Lambda + H_L) A h_1 d\xi_1. \tag{14}$$

Equations (11)-(14) are differenced on a Lagrangian grid where ρ, ρ_e, ε_i, ε_e, p_i, and p_e are carried at the cell centers and v is carried at the cell interfaces. There are as many of the above equations as there are cells in the whole grid and the limits of integration for the continuity and internal energy equations are the cell interfaces, while the limits are the cell centers for the momentum equation. The differencing is second order in space and a two step predictor-corrector scheme is used for the temporal advance.

Identifying the kinetic energy of cell J+1/2 with interfaces at ξ_J and ξ_{J+1} as

$$\frac{1}{4} M_{J+1/2}(v^2_{J+1} + v^2_J),$$

one can show through a lengthy algebraic computation that the differencing scheme conserves total energy even though the internal energy is transported. This is valid as long as the velocities at the boundary interfaces are zero.

Due to the large change in volume during the experiment from the target dimensions (a few microns) to the blast wave formation (~1 cm), it is necessary to rezone the grid. This is done each time step by first determining the cells which provide the most stringent Courant condition. An isolated subset of these cells is chosen and the interface between each selected cell and its neighbor is moved in such a way as to relax the Courant condition. The amount by which the interface is moved is determined by conserving total mass, linear momentum and energy.

Finally, we mention that the different terms in the above equations are handled in a time split fashion. The hydrodynamics, including the artificial viscosity are done first, then the thermal conduction and equilibration terms are solved implicitly each time step. With these terms completed the chemical reactions are next computed using an improved ARIS[6] module, and finally the radiation is transported.

B. Geometry.

The initial configuration of the experiment is a thin, planar disc target which is hit on one side with a laser beam. The blowoff from the ablation then undergoes a divergent expansion into the background gas. Even though the code is one dimensional, i.e., the variables depend on only one coordinate, one would like to properly treat both the initial configuration and the divergent blowoff. Clearly a Cartesian geometry can handle the planar target but not the divergent blowoff. A spherical geometry, as usec by Stellingwerf[7] in the code MACH1 to model the laser target interaction, does account for the divergent expansion, but it has other problems. Given that the target material expands in a cone of half-angle θ_o, it is impossible for the section of the sphere representing the target to simultaneously have the same area, total mass, density and thickness of the actual target. Moreover, the most limiting factor is the inability of a spherical geometry to account for the acceleration and divergence of the rear side of the target after the laser radiation has been absorbed. In such a geometry the rear side implodes toward the center of the coordinate system. Shadowgraphs clearly show that the rear side blowoff is quite different from that of the front side and it is therefore of interest to model.

A spheroidal oblate coordinate system offers the advantage of both a planar initial target and a spherical, divergent expansion. Such a coordinate system can be generated by drawing ellipses in a plane perpendicular to the target face. These ellipses converge to a bar at the target face and tend toward a circle far from the target. The orthogonal set of coordinate lines have an hourglass shape near the target and become spherical rays at large distances. These generating lines are then rotated about an axis through the center of the disc. The axis represents the path of the laser beam. One of these hourglass-shaped generating lines is chosen

as the lateral boundary of the expanding material. Figure 1 is a sketch of the geometry and initial configuration. The coordinate transformation to cartesian coordinates is given by

$$x = (s^2 + a^2)^{1/2}\cos\psi\,\cos\phi\ ,$$

$$y = (s^2 + a^2)^{1/2}\cos\psi\,\sin\phi\ ,$$

and

$$z = s\,\sin\psi, \tag{15}$$

where $0 \leq s < \infty$, $-\pi/2 \leq \psi \leq \pi/2$, and $0 \leq \phi \leq 2\pi$. In terms of the discussion of oblate spheroidal coordinates given by Arfken[8], $s = a\,\sinh(u)$. The flow variables are taken to depend on the distance s and a fixed ψ_o determines the hourglass-shaped lateral boundary. From early observations of the experiment, the major portion of the target material expands into a cone of half-angle 40^o. Thus $\psi_o = 40^o$, and the radius of the target disc (r_t) that is irradiated by the laser is related to the parameter a by

$$r_t = a(1-\sin^2\psi_o)^{1/2}\ . \tag{16}$$

The corresponding scale factors are

$$h_s = (s^2 + a^2\sin^2\psi\ )^{1/2}/(s^2 + a^2)^{1/2}\ ,$$

$$h_\psi = (s^2 + a^2\sin^2\psi\ )^{1/2}\ ,$$

and

$$h_\phi = (s^2 + a^2)^{1/2}\,\cos\psi\ . \tag{17}$$

From these the elemental area and volume are given by

$$A(s) = \int_{\psi_o}^{\pi/2} d\psi \int_0^{2\pi} d\phi \; h_\psi h_\phi \;,$$

$$= \pi a (s^2+a^2)^{1/2} \left[(1+s^2/a^2)^{1/2} - \sin\psi_o (\sin^2\psi_o + s^2/a^2)^{1/2} \right.$$

$$\left. - \frac{s^2}{a^2} \ln \left[\frac{\sin\psi_o + (\sin^2\psi_o + s^2/a^2)^{1/2}}{1 + (1 + s^2/a^2)^{1/2}} \right] \right] , \quad (18)$$

and

$$Vol = \int_{s_1}^{s_2} ds \int_{\psi_o}^{\pi/2} d\psi \int_0^{2\pi} d\phi \; h_s h_\psi h_\phi \;,$$

$$= \frac{2\pi}{3} \left[(s_2^3 - s_1^3)(1 - \sin\psi_o) + a^2 (s_2 - s_1)(1 - \sin^2\psi_o) \right] . \quad (19)$$

C. Thermal Conduction.

The electron thermal conduction has long been known to present a problem in laser-target interactions[9]. The difficulty lies in the fact that the temperature gradient length scale $L_T = |d\ell n(T_e)/dx|$ is on the order of the mean free path λ near the critical surface, while the classical formula for the thermal conductivity assumes $\lambda/L_T << 1$. The usual approach in fluid codes to rectify this problem has been to limit the heat flux q such that

$$q = \min \{ -\kappa_{cl} \nabla T_e, \; -q_{fs} \, sign(\nabla T_e) \}, \quad (20)$$

where κ_{cl} is the classical or Spitzer-Harm conductivity, and q_{fs} is the free streaming limit for thermal heat flux, $q_{fs} = \alpha n_e k_B T_e (k_B T_e/m_e)^{1/2}$ with typically $0.03 < \alpha < 0.1$. A smooth variation in the heat flux can be achieved by using instead

$$q = - \frac{\kappa}{1 + \kappa |\nabla T_e|/q_{fs}} \nabla T_e \ , \tag{21}$$

with $\kappa = \kappa_{cl}$.

It has also been shown by Manheimer[11] that the heat flux can be reduced by turbulence through ion acoustic waves. For $T_i \ll T_e$, these waves are driven unstable by the return current of an anisotropic electron distribution function. The criterion for instability can be written as[12]

$$q > F = \frac{3}{2} n_e k_B T_e \left(\frac{k_B T_e}{m_e}\right)^{1/2} \left\{ (1+3T_i/T_e)^{1/2} \left(\frac{m_e}{m_i}\right)^{1/2} \right.$$

$$\left. + \left(\frac{T_e}{T_i}\right)^{1/2} \left[(1+3T_i/T_e)^{1/2} - (T_i/T_e)^{1/2}\right] \exp\left(- \frac{T_e/T_i + 1.5}{1.25}\right) \right\}, \tag{22}$$

When this condition is satisfied the heat flux can be written as[11]

$$q = - \frac{\kappa_{cl}}{1 + \kappa_{cl}/\kappa_{an}} \nabla T_e \ , \tag{23}$$

where κ_{an} is the anomalous thermal conductivity due to the turbulence and is given by

$$\frac{\kappa_{cl}}{\kappa_{an}} = \psi = f(Z) \frac{3\pi^2}{2} \frac{n_e \lambda_{De}}{\ell n \Lambda} \left(\frac{e\phi}{k_B T_e}\right)^2 \ , \tag{24}$$

with f(Z) a function of the mean charge state Z, λ_{De} is the Debye length, and ϕ the potential fluctuations due to the turbulence. The instability saturates by ion trapping with the maximum fluctuation

$$\frac{e\phi_{max}}{k_B T_e} = \frac{1}{4}\left(\frac{1}{1.25} - 3\,\frac{T_i}{T_e}\right)^2 . \qquad (25)$$

The procedure we use to determine instability is more efficient than that described in Ref. 11 or Ref. 12. From eqns.(22) and (23) we first determine the sign of $\alpha = q_{cl}/F - 1$, where $q_{cl} = \kappa_{cl}\nabla T_e$ and F is defined in eqn.(22). If $\alpha \leq 0$, then the waves are stable and $\kappa = \kappa_{cl}$. On the other hand, if α is positive then the instability is operative. Next the magnitude of the fluctuations is found by setting $\psi = \min(q_{cl} - 1, \psi_{max})$, where ψ_{max} is given by eqn.(24) using eqn.(25). This procedure accounts for the saturation in the growth of the unstable waves and gives the marginal stability condition otherwise.

The effect of saturation of the heat flux in steep temperature gradients must still be included, so once having found the value of κ_{cl}/κ_{an} we use $\kappa = \kappa_{cl}/(1 + \kappa_{cl}/\kappa_{an})$ in eqn.(21). In the running of the code it was found that the heat flux saturated near the critical surface but the ion acoustic instability was stable there due to the fast thermal equilibration times. At and in front of the blast wave where the thermal conduction leads to a leading electron temperature foot, the electron heat flux was limited by ion acoustic turbulence as well as being saturated.

A third effect related to the heat flux is its non-local nature in extreme temperature gradients. This aspect has been discussed by Luciani, et al.[13], but was not included in the present code. Further work on this problem in the presence of large density changes is needed before their expression for the heat flux can be used in the present simulation.

We finally mention that ion heat flux is included in the code and the effect of saturation is treated in a similar manner to that of the electron heat flux. We did not consider any instability which could limit the ion heat flux by turbulence.

D. Equation Of State.

The equation of state is different from that of an ideal gas law only in the target material while it remains a solid prior to vaporization. Although the energy required to completely vaporize the target foil is very small compared to the total laser energy in the experiment, neglect of a realistic equation of state for the solid target leads to absurd compressions in the rear side of the target. We do not use a detailed model or table for the solid equation of state, for this would require spending an excessive amount of computer time on transient phenomena. Rather we employ a simple analytic model which adequately accounts for the dominant physical effect, namely the rapid rise in the sound speed in a compressed solid.

The total pressure can be written as[14]

$$p = p_c + p_n + p_e \ , \tag{26}$$

where subscript c refers to the zero temperature isotherm or cold, solid component, subcript n to the nucleon component (neutrals or ions), and subscript e to the electron component. Let ρ_{oo} be the density of the solid at zero temperature and $\eta = \rho/\rho_{oo}$, then the internal energy and pressure are related by

$$\varepsilon_c = \frac{1}{\rho_{oo}} \int_1^\eta p_c \eta^{-2} d\eta \ . \tag{27}$$

Based on formulas (3.4) and (3.20) in Ref.14 we employ the following expressions for the cold pressure:

$$P_c = \begin{cases} C_{32}(\eta^{5/3} - 1) & , \eta \geq 1 \\ C_4 \eta^{2/3}\left[e^{C_5(1-\eta^{-1/3})} - e^{C_6(1-\eta^{-1/3})} \right] & , \eta \leq 1, \end{cases} \quad (28)$$

where for aluminum $C_{32} = 4.4\times10^{+11}$ ergs/cm^3, $C_5 = 7.22$, $C_6 = 3.14$, and $\rho_{oo} = 2.71$ g/cm^3. The value of C_4 was taken to be much smaller than $6.1\times10^{+11}$ ergs/cm^3 of Ref. 14, namely, $C_4 = 1\times10^{+7}$ ergs/cm^3. As can be seen in the P-V-T diagram for aluminum in Fig. D-8 of Ref. 14, there is a deep but narrow well of negative pressure for η slightly less than 1. This feature represents the intramolecular forces which bind a solid together. A large negative pressure can lead to numerical instabilities unless exceedingly small time steps are used. Since the phase of negative pressures is transitory and the internal energy associated with the well is small we can reduce the depth of the pressure well without seriously altering the physics. Further, as the target rarefies due to heating the thermal pressure terms in eqn.(26) readily dominate. From eqns.(27) and (28) and the coefficients C_4, C_5, C_6 from Ref. 14, one finds that the zero temperature sublimation energy for the target geometry of Fig. 1 is $8.3\times10^{+4}$ ergs, which is much less than the 23 Joules deposited by the laser.

The steep rise of the pressure for compressions does play a significant role in the propagation of shocks through the solid target. In agreement with the results of Schmalz and Meyer-ter-Vehn[15] who used a detailed equation of state, we also found a series of shocks in the target during the early stages of disassembly. These shocks display a small density jump but large pressure changes.

The other terms in eqn.(26) are treated according to the ideal gas law, except initially when the temperature is < 0.1 ev. The P-V-T diagram indicates a constant, low pressure for low temperatures and $\eta < 1$. In these regions the pressure in the solid is taken to be that of the initial ambient gas. This is reasonable since the foil and background gas are in equilibrium before the laser is turned on, while the temperature rapidly increases afterwards.

E. Radiation.

We begin with a discussion of the initial radiation in the problem, that of the incident laser. The total energy in the laser pulse was set at 23 Joules and a Gaussian shape of 4 nsec full-width half-maximum was adopted. The laser wavelength was 1.06 μm, modeling the output from a neodymium glass laser. The peak intensity of the pulse was $1\times10^{+13}$ W/cm^2 and occured 5 nsec after the start of the calculation. The pulse was cut off at 10 nsec. The beam energy was deposited using the 1-D radiative transfer equation with inverse bremsstrahlung absorption:

$$\kappa_{IB} = \frac{(\omega_{pe}/\omega_L)^2}{c\tau_e[1 - (\omega_{pe}/\omega_L)^2]^{1/2}} \quad , \tag{29}$$

where ω_{pe} is the electron plasma frequency, τ_e is the electron-ion collision time, and ω_L is the laser frequency. Since the radius of the beam was that of the target disc (r_d), the heating rate per unit volume for the electrons in cell J is

$$H_L = \pi r_d^2 I_{J+1}(1 - e^{-\kappa_{IB}(J)\Delta_J}) \frac{1}{Vol(J)} , \qquad (30)$$

where I_{j+1} is the mean intensity entering cell J of thickness Δ_j. The fractional ionization at the front edge of the target is artificially increased at the initial instant of the simulation to provide free electrons. This ensures the absorption of the laser beam since inverse bremsstrahlung depends on the presence free electrons. For simplicity, we neglect reflection of the laser radiation and deposit any remaining incident radiation not absorbed before the critical surface into that cell containing the critical surface. The critical surface is defined as the position where the denominator of eqn.(29) vanishes.

The radiation from the heated gas is treated in several ways. First, bremsstrahlung and recombination radiation are calculated for both the target aluminum material and the ambient nitrogen gas. The recombination radiation is assumed to have a Planck-like spectrum with an effective temperature T_{rad}. For cell J this quantity is determined by equating the energy density of a blackbody at T_{rad} with the energy emitted by recombination radiation in cell J. Radiation emitted by the nitrogen gas is treated as optically thin, i.e., an energy loss. However, radiation from the aluminum is transported through the entire grid. The radiation transport is calculated by the standard ray-tracing technique in the forward and rearward direction. As shown in the detailed paper by Duston et al.[16], radiation is a major source of heating for the rear side of the target foil. Hence, since one of our objectives is to simulate the rearward blowoff, it is imperative to correctly calculate the basic energy transport through the entire target. The radiated energy is divided into twelve frequency bins which are chosen to resolve the inner-shell absorption edges of aluminum. The absorption cross sections are from Fig. 2 of Ref. 16. Any radiation that passes through the aluminum gas is

also transported through the ambient nitrogen gas. This results in the dissociation of background N_2. The absorption cross sections for this process are based on those used in Hyman et al.[17]

Second, excitation line radiation is modelled in two extreme conditions: completely optically thick and optically thin. The optically thick case simply means that any emitted line from a cell J is absorbed in that same cell. No calculation is needed here. For the optically thin case we calculate the emission from 18 resonance lines of aluminum and 14 resonance lines of nitrogen. All ionization stages of both species are covered. Our interest in the line radiation stems from the possibility of cooling in the cavity behind the blast wave. We did not consider the K-lines which originate during the early phase of target vaporization. In calculating the emission from our chosen set of lines, the excited state populations are determined by balancing the collisional excitation rate against the de-excitation rate from the excited state, the ionization rate to the next higher ionization stage, and the radiative decay rate. Optical pumping as well as photoionization of the resonant state due to recombination radiation are not evaluated. These features ensure that the line radiation is not overestimated in the absence of reabsorption.

F. Chemistry.

Much effort was spent in developing a chemistry module which can handle the extreme range of chemical conditions in the experiment. For simplicity, we do not follow any excited state populations but assume all ions (and neutrals) are in the ground state. Essentially we divided the chemical evolution of the aluminum material into three schemes. First, during a brief initial stage the aluminum undergoes a phase transition from a solid to a

high density gas at $\leq$ 1 ev. Here we use an analytic procedure to determine the temperature and fractional ionization from the internal energy. The analytic solution is based on fits to numerical calculations of an equilibrium aluminum gas with only neutral and singly ionized species. As the target continues to absorb the laser energy, the fractional ionization and temperature drastically increase. Once the fractional ionization increases above 0.8, an iteration on the temperature and ionization level for a given internal energy is employed, again for equilibrium conditions. In this second scheme for the chemical evolution all the ground state ionization levels are included. Finally, when the electron density in any cell falls below $5.\times10^{+19}$ cm^{-3}, the chemistry in that cell is integrated in time using reaction rates, i.e., we allow the population of the ground state levels to fall out of equilibrium. For this third scheme, the ARIS[6] module is used to solve the corresponding set of stiff differential equations. For the nitrogen gas, the chemical evolution is always followed using reaction rates.

The numerical details of this evolution from low temperature, dense equilibrium chemistry to high temperature, rarefied reaction rate chemistry is too complicated to be reported here. We do mention that the transition from one chemistry scheme to the next must be done smoothly. This requires the inclusion of many reaction processes to ensure that the limiting conditions lead to equilibrium results. For instance, at high density and low temperature we reproduce the simple Saha equilibrium by using detailed balance between collisional ionization and 3-body recombination. Such equilibrium is valid only for a high density gas where the dominant recombination process is 3-body. In addition to 3-body recombinations and electron collisional ionization, we also include radiative recombination and dielectronic recombination processes so that the lower density, higher temperature regimes are modeled correctly. A high density correction for

dielectronic recombination rates similar to that used by Jordan[24] is employed.

As an aside on computational physics, the use of a sequence of numerical schemes for the chemistry is most efficiently and correctly employed in a Lagrangian hydrodynamic code. In this approach the decision to switch from one scheme to the next, viz., analytic -> equilibrium -> time dependent, can be made in each individual cell independent of all the others since each cell carries the same material with it. Unfortunately, in a purely Lagrangian code the effects of charge exchange cannot be investigated, for the aluminum debris cannot overrun the nitrogen background. We must thereby limit the simulation results to the high pressure regime where strong coupling between the expanding debris and background occurs.

III. SAMPLE RUNS

In this section we will present detailed graphical results from the numerical simulations. Four distinct models were studied. The differences in the models lies in the treatment of the chemistry and line radiation. In model A, which we refer to as the standard model, time dependent chemistry is employed and all line radiation is assumed to be optically thick, i.e., no transport of line radiation is considered. In model B, equilibrium chemistry is used and again the line radiation is optically thick. For models C and D the line radiation is taken to be optically thin, but model C has time dependent chemistry and model D has equilibrium chemistry. Recall from section II.F. that equilibrium chemistry is not necessarily LTE but includes the effects of radiative and dielectronic recombination. The objective of studying these four models is: (i), to demonstrate the importance of non-equilibrium chemistry, and (ii), to investigate whether line radiation can realistically cool the cavity inside the blast wave. Since we do not perform a detailed calculation for the transfer of line radiation, the two extremes of optically thick and thin enable one to obtain only qualitative conclusions.

A. Standard Model.

Figure 2 shows the position of the blast wave for both the front side and the back side as a function of time for model A, the standard model. The time in this figure is measured from the instant of peak intensity of the laser pulse, which is what the experimentalists use as their zero time. In the code the laser pulse is initiated 5 nsec before the peak. The solid line in Fig. 2 is given by

$$R(\text{cm}) = 0.123 \left[\frac{E(\text{Joules})}{p(\text{Torr})} \right]^{0.2} [t(\text{nsec})]^{0.4} \qquad (31)$$

for E = 23 Joules and p = 2.5 Torr. This equation is from Ref. 3 and describes the observed temporal evolution of the front side of the blast wave. As noted in that reference, the equation for R(t) has the same temporal and parameter dependence as that for a Taylor-Sedov blast wave. We note the excellent agreement in Fig. 2 between the numerical simulation and the experimental data for the position of the front side blast wave. The blast wave on the back side displays a turbulent structure in the shadowgraphs and no general formula for its position in time has been developed. This turbulent structure will be discussed below in light of the results of the simulation. The equal mass radii (R_{EM}) for both the front and back side are also noted in Fig. 2. Specifically, 0.15×10^{-6} g is ablated toward the front side while the remaining 0.55×10^{-6} g is accelerated rearward. As demonstrated by the simulation, the Taylor-Sedov blast wave solution becomes applicable for the front side shock location only after several equal mass radii have been encountered.

In Fig. 3 the energy budget for model A is presented. $\int E_L dt$ is the accumulated energy deposited by the laser over time. It attains 23 Joules at 10 nsec after the peak of the laser pulse. E_K is the instantaneous kinetic energy of directed motion while E_T is the instantaneous thermal (random) energy of all particles. The chemical energy, i.e., the energy locked up in the ionization of aluminum and nitrogen at a given time is denoted by E_C. Finally, $\int E_R dt$ is the accumulated energy lost from the system during the run due to recombination and bremsstrahlung radiation. The values in Fig. 3 include both sides of the expanding target. The relation

$$E_K(t) + E_T(t) + E_C(t) + \int_{-5\ \text{nsec}}^{t} \dot{E}_R dt = \int_{-5\ \text{nsec}}^{t} \dot{E}_L dt \ ,$$

expressing conservation of total energy, is satified to within 3% throughout the run. This result is also typical for the other runs dicussed below. Nearly all of the energy that is missing during a simulation run occured in the time dependent chemistry routine.

Note in Fig. 3 that initially the kinetic energy is dominant, but after ~ +20 nsec the fraction in thermal energy is largest and stays at roughly 35%. For an adiabatic Taylor-Sedov blast wave with $\gamma = 1.1$ (see ref. 3) 90% of the total energy is thermal with the rest being kinetic. This is clearly not the case here and points to the first major difference between the simulation of the experiment and the ideal blast wave theory. This difference is due to the significant amount of energy locked up in ionization potential and the smaller radiated energy. These two energy sinks, which are not included in the ideal Taylor-Sedov model, account for roughly 45% of the total energy in the system. The high fraction of kinetic energy at the end of the run, 20% instead of 10%, arises from the fact that the rear side blowoff is dense and relatively cool.

Figures 4a through 4g show snapshot profiles of different quantities during the standard model simulation. The figure captions fully describe the nomenclature and symbols used to present the numerical data. Here we will point out a few salient features.

Note first of all that the time shown on the graphs refers to the simulation time which is zero when the laser turns on. To transform to the time from the peak intensity of the laser pulse subtract 5 nsec. Figure 4a displays the situation at the initial instant of the simulation; the aluminum is at solid density of $6\times10^{+23}$ atoms/cm^3 and the ambient nitrogen is at $3.5\times10^{+17}$ molecules/cm^3. Both materials are predominantly neutral, but a thin partially ionized region at the front of the target is imposed to ensure that the laser beam is absorbed by inverse bremsstrahlung. Note that the

abscissa is in Lagrangian cell units in order to expand the target region for clarity.

Figures 4b, 4c, and 4d display the situation shortly after the peak of the laser pulse again in Lagrangian cell units. The critical surface occurs near the peak of the electron density and temperature (see Fig. 4b). One can clearly see, from the plot of the artificial viscous pressure Q, a series of shocks traversing the aluminum target. This feature agrees with the detailed equation of state study of Ref. 15. The heating of the back side of the target is due to these shocks as well as to the absorption of radiation emitted from a region near the critical surface. The graph of the mean charge state in Fig. 4c, $n_e/(n_i + n_n)$, shows that highly ionized aluminum, namely Al^{+9}, Al^{+10}, and Al^{+11}, is created early on in the laser target interaction. We find that during the subsequent stages of forward blowoff and cavity formation the aluminum does not have enough time to recombine and remains in these highly ionized states. Since the cavity temperature drops below 100 ev, this non-equilibrium ionization structure points out the importance of using a non-LTE, time dependent chemistry in the simulation. The spectrum in Fig. 4d only includes the radiation from recombination and bremsstrahlung; it displays some of the qualitative features of Figure 11 in Ref.16 but clearly the lack of a detailed treatment of the recombination spectrum and lines represents a limitation of our present model.

Figure 4e is a snapshot of the flow variables at the time when the forward moving blowoff has swept up one equal mass of ambient material. The abscissa is now given in physical space since the target has expanded sufficiently to be resolved. The formation of a reverse shock at this time on this front side can be seen from the peak in the artificial viscosity (Q) in the aluminum material. Note that radiation and thermal conduction have raised the electron temperature of the ambient nitrogen on the front side and a thermal foot leading the main shock is present there.

Figures 4f and 4g show the long time development of the system out till the forward moving blast wave reaches the boundary of the calculational grid. From the density plot in Fig. 4f one finds that the blast wave thickness, as measured by the width of the peak in the electron density profile, is roughly twice as thick as the experimentally observed value of 3% of the blast wave radius[3]. However, the peak electron density in the shock of $4\times10^{+18}$ cm^{-3} is typical of the reported measurements from several interferograms[18]. Moreover, the mean electron density in the cavity of a few times 10^{+17} cm^{-3} is in good agreement with the recent, though tentative, measured value of $2\times10^{+17}$ cm^{-3} at 60 nsec after the peak of the laser pulse[19]. The surprisingly high value for the electron density reflects the high degree of ionization of the aluminum debris in the cavity; note that the ion density in the cavity is much smaller. From the viscous pressure plot in Fig. 4f the reverse shock on the front side has moved back toward the original target position and the formation of a second reverse shock in the backward moving aluminum is also evident. By the time of Fig. 4g the cavity between the forward and backward moving blast waves is nearly isothermal with T_e - 60 ev. This is the second major difference of the simulation results from the ideal, adiabatic Taylor-Sedov blast wave wherein the temperature rises as one moves inward from the blast wave. Actually the run of the velocity and ion density on the front side looks quite like the solution for an <u>isothermal</u> Taylor-Sedov blast wave as discussed in Ref. 20. The isothermality is mainly due to electron thermal conduction. We note for reference that an isothermal blast wave also evolves according to a $t^{0.4}$ law.

B. Comparisons With Other Models.

Figures 5a, 5b, and 5c show snapshots of the flow variables for models B, C, and D, respectively. Each of these graphs is at a time close to 50

nsec in simulation time and can be compared with Fig. 4f. The distinction between these models and the standard one (model A) is noted in Table I which contains some of the gross characteristics for each model. The figures and table will be discussed together. The main differences between the time-dependent (model A) and equilibrium chemistry (model B) are the lower electron temperature in the cavity (65 ev for model A vs. 90 ev for model B) and the higher mean ionization level in the cavity (9.7 for model A vs. 7.5 for model B). These differences arise because the equilibrium model allows sharing between ionization and thermal energy with no regard for time scales. When we assume that the radiation from the resonance lines is optically thin, as in models C and D, we find a significant increase in the percentage of radiation lost from the system. The values of 61% and 38% are much higher than the experimentally estimated 25% radiation energy loss when the MRC gas mixture was used for the ambient material. Since the MRC mixture is a much more efficient radiator than a pure nitrogen gas we surmise that the resonance lines cannot be optically thin. Simple estimates for the optical depth of a Doppler broadened line also show that the optical depth is greater than one for the cavity conditions. Furthermore, Figs. 5b and 5c indicate too thin a blast wave and too high a peak electron density, when compared against the observations. This is especially true for model C.

TABLE I

COMPARISON OF DIFFERENT MODELS

(E_L = 23 Joules, p_o = 2.5 Torr, t - 50 nsec)

		A Time dep. chem. No line rad.	B Equil. chem. No line rad.	C Time dep. chem. Line rad.	D Equil. chem. Line rad.
Energy	E_K	23%	24%	16%	23%
Budget:	E_T	37%	35%	11%	23%
	E_C	21%	21%	12%	15%
	E_R	19%	20%	61%	38%
Shock:	R(cm)	0.90	0.89	0.88	0.86
	$n_e(cm^{-3})$	$4\times10^{+18}$	$6\times10^{+18}$	$18\times10^{+18}$	$10\times10^{+18}$
Cavity:	T(ev)	65	90	30	70
	$n_e(cm^{-3})$	$2\times10^{+17}$	$2\times10^{+17}$	$1.5\times10^{+17}$	$2\times10^{+17}$
	n_e/n_{Al}	9.7	7.5	9.7	7.0
	n_e/n_N	4.5-5	4.5-5	3-4.5	3-4.5

C. Further Results.

The experimentally observed floculli on the backside blowoff is very distinct from the smooth front side. Within the confines of a one dimensional calculation it is impossible to model such turbulence; however, we find that the conditions for a Rayleigh-Taylor instability are satisfied in the back side blast wave. It is possible that such an instability leads to the observed structure and we present the numerical results of a linear analysis below.

Specifically, the Rayleigh-Taylor instability arises from the deceleration of the aluminum debris by the less dense ambient nitrogen. This deceleration occurs when the rearward moving debris has swept up about an equal mass of the ambient material. The growth rate for the decelerating Rayleigh-Taylor instability is given by

$$\omega = \left[\frac{DV}{Dt} \cdot \nabla \ln(\rho) \right]^{1/2} , \qquad (32)$$

where ω is the growth rate. This expression is calculated at each interface between cells and the expression for the temporal velocity derivative includes the pressure gradients and the artificial viscosity terms in eqn.(12). Whenever ω is real the interface is unstable. The resultant growth rates (ω real) for four different times in the standard model are presented in Figure 6. At an early phase in the simulation the front side contact discontinuity, located at the right vertical line near cell #41, is seen to be unstable. However the duration of the conditions for a positive growth rate last only a couple of e-folding times, and by 55 nsec the front contact discontinuity is essentially stable. (Isolated crosses are not considered to be indicative of consistent conditions for Rayleigh-Taylor growth but rather transient phenomena.) On the other hand, from roughly 20 nsec to at least 55 nsec the rearside contact discontinuity, at the left

vertical line near cell #20, is Rayleigh-Taylor unstable. This temporal duration is sufficient for several e-folding times. As can be seen from Fig. 2, this time span centers around the time of one equal mass radius for the back side blowoff. We suggest that the flocculi observed in the shadowgraphs at ~ 50 nsec and beyond are due to this Rayleigh-Taylor deceleration instability. The continuation of the turbulence into late times emerges from the sufficient number of e-folding times for this instablility on the rear side. At very early times, say 10 to 20 nsec, the front side may also exhibit some structure, but the limited number of e-folding times for this region would not lead to non-linear effects.

For completeness, we display the local Mach number at four different times for the standard model in Figure 7. The results are related to the proposed use of small obstacles as a probe of the cavity dynamics[21]. Beyond about 20 nsec the major portion of the cavity between the forward and backward moving blast waves is subsonic. This result predicts that a bow shock formed about a small obstacle at the time it is overrun by the forward moving blast wave will dissipate into a sound wave as the expansion continues.

IV. SUMMARY

We have presented the details of a one dimensional numerical simulation code intended to model the NRL laser/HANE experiment in the high pressure regime (p_o > 1 Torr). Although the code is one dimensional and cannot model the development of instabilities and the self-generated magnetic fields, a large number of physical processes have been modeled in order to study the gross physical characteristics of the experiment. These features include an oblate spheroidal geometry to account for the rearward expansion, electron and ion thermal conduction with saturation including the limiting effects of

the ion-acoustic instability on electron thermal conduction, an equation of state representative of solid aluminum during the target dissasembly, radiation transfer for the continuum and bremsstrahlung radiation originating in the aluminum material, and an intricate chemistry which spans the range from LTE to highly non-equilibrium conditions.

Other numerical codes have studied the laser-target interaction problem in 2-D with accurate radiation transport and/or self-generated magnetic fields, such as that of Colombant, et al.[25], Brackbill and Goldman[26], and Pert[27]. These codes are constructed to simulate the first few hundred picoseconds of the interaction, before any hydrodynamic reaction of the background plasma. The emphasis of the present laser/HANE experiment is primarily on the coupling of the debris to the background gas which takes place over a timescale of tens of nanoseconds. The code we have described concentrates on the latter, longer timescale phenomena, and hence is significantly different from the previous codes. For instance, the use of a Lagrangian grid or adaptive rezoning is necessary to follow the great change in length scales from the target size to one centimeter: the above referenced codes employed a fixed Eulerian grid for the hydrodynamics. The extension of the present numerical techniques to a 2-D code is clearly necessary to improve the radiation transport, to study instabilities, and to include the effects of the self-generated magnetic field on thermal conduction. The present model is an initial step toward a more complex 2-D one and the results, listed below, point out specific features which a more advenced code should further study.

The primary results from the present numerical simulation are as follows.

(1) For the standard model (A) the cavity behind the forward moving blast wave is hot (T_e - 60 ev) and dense (n_e - $2\times10^{+17}$ cm^{-3}). The ion temperature in the cavity is about the same as T_e but the ion density in the

aluminum part of the cavity is a factor of 10 smaller (see Fig. 4f). Overall, the dynamic structure of the forward blowoff region resembles an isothermal Taylor-Sedov blast wave, albeit with a significant amount of energy tied up in chemical potential and radiation losses (see Fig. 3). This result is quite different from the LTE model presented by R. Stellingwerf[22] wherein the cavity is much colder (T_e - few ev) and rarefied (n_i - few $\times 10^{15}$ cm^{-3}). Our predicted electron density for the cavity agrees with a tentative measurement by J. Stamper[19]. The electron densities in the blast wave also agree with the measurements[18].

(ii) Due to the initial rapid heating and the slow recombination rates, the material in the cavity is highly overionized for the local electron temperature. In particular, by 50 nsec the aluminum is mostly $A\ell^{+9}$, $A\ell^{+10}$, and $A\ell^{+11}$, and the nitrogen is mostly N^{+5} (see Table I). The latter has been observed in an integrated spectrum[23] and it should be possible to search for the presence of $A\ell^{+10}$ using the same technique. Such an observation would provide a direct verification of our use of a time-dependent chemistry. Due to the limitation of a Lagrangian code, we did not include charge exchange as one of the chemical reactions. If the blast wave becomes leaky for lower ambient pressures (p_o < 1 Torr), some of these highly ionized particles could penetrate ahead of the blast wave. To model charge exchange and leaky blast waves a two ion fluid code or a particle code would be needed.

(iii) The results of our models which assume optically thin lines (models C and D) indicate an unrealistically large amount of radiation loss (see Table I). This suggests that the resonance lines from the blast wave and cavity are not optically thin, but an improved radiation model with line transport is required to determine how thick the lines are.

(iv) The deceleration Rayleigh-Taylor instability is found to be satisfied at the rear contact discontinuity at the time when an equal mass is

swept up by the rearward moving blast wave (see Fig. 6). We suggest that this instability may be responsible for the flocculi observed on the rear side. Again, a two dimensional code is required to follow the non-linear development of the unstable regions. On the front side the instability is also active, but only for a brief time near 7 - 20 nsec. This span of time allows only a few e-folding times. It would be of interest to take shadowgraph pictures at these early times to discern if the blast wave is initially unstable but later heals itself to the smooth form seen in shadowgraphs at times > 50 nsec. It should be noted that this instability appears to have little to do with the formation of the prominent aneurisms seen on the front side blast wave.

(v) Due to the high temperature in the forward half of the cavity the flow is subsonic. A bow shock formed about a small, stationary obstacle to the blast wave would be expected to dissipate into a sound wave with a weaker density jump as the obstacle is engulfed by the expanding cavity.

ACKNOWLEDGMENTS

We are grateful to Dr. Ellis Hyman for continued encouragement during the course of the code development and for a detailed reading of an initial draft of this paper. Conversations with Drs. Ed McLean, Chuck Manka and John Stamper were fruitful in focusing our efforts on specific issues. Advice from Dr. Robert Clark on radiation transport and from Dr. John Gardner on the equation of state were particularly helpful. We are especially thankful to Dr. Barry Ripin for his support during this project. This research was funded by the Defense Nuclear Agency.

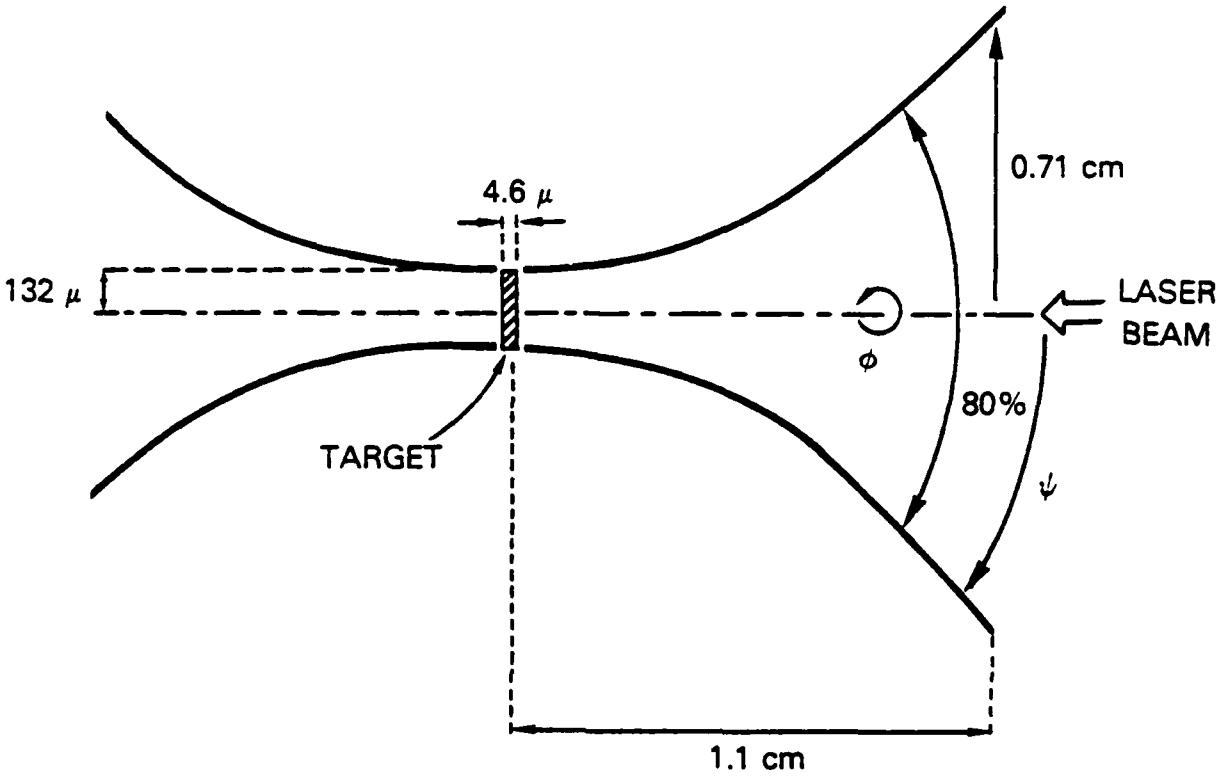

Figure 1. Geometry of target, laser beam, and boundary of oblate spheroidal coordinate system used in the numerical simulation. The system is rotationally symmetric about the laser beam axis. The opening angle for the blowoff asymptotically approaches 80° far from the target. The front and back boundary are each 1.1 cm from the target. The target is a disc of radius 132 μ and thickness 4.6 μ.

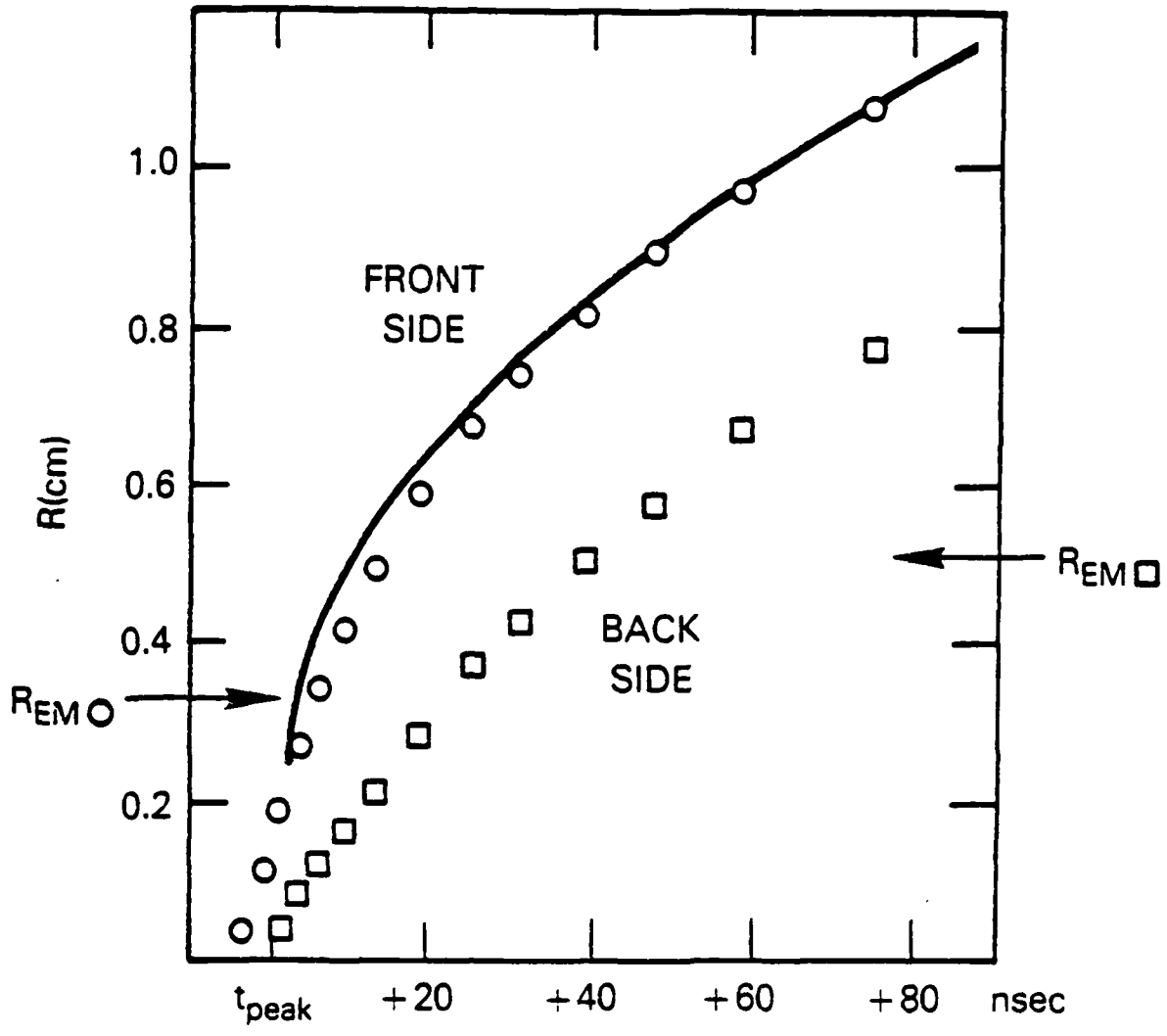

Figure 2. The position of the front side (o) and back side ([]) blast wave for the standard model as a function of time measured from the peak intensity of the laser pulse. The equal mass radii for both sides are also indicated. The solid line is the position of the front side blast wave from the experimental.

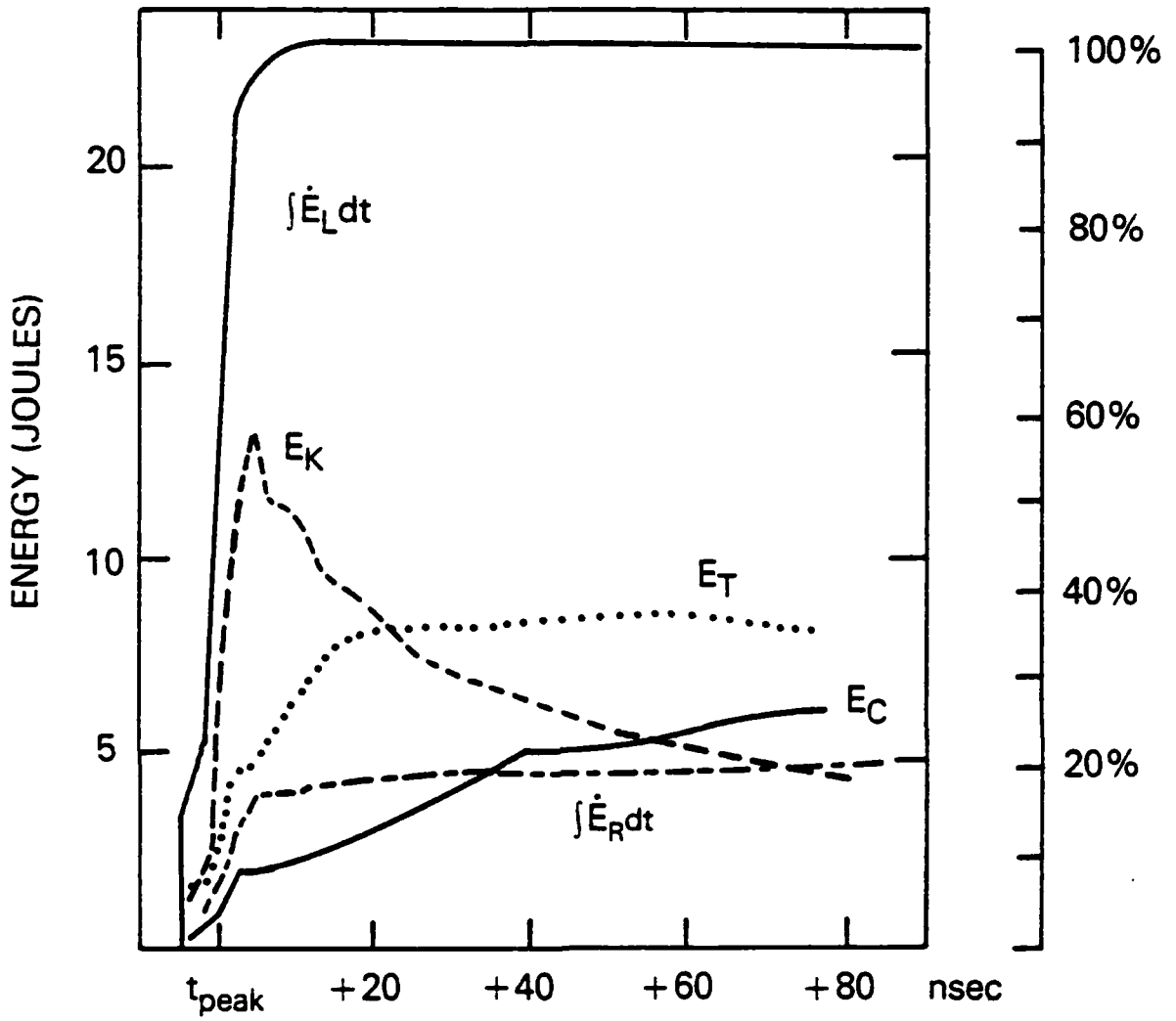

Figure 3. The energy budget for the standard model as a function of time measured from the peak intensity of the laser pulse. $\int \dot{E}_L dt$ is the accumulated energy input from the laser, E_K is the instantaneous kinetic energy of directed motion, E_T is the thermal energy of random motion, E_C is the chemical potential energy, and $\int \dot{E}_R dt$ is the accumulated radiated energy.

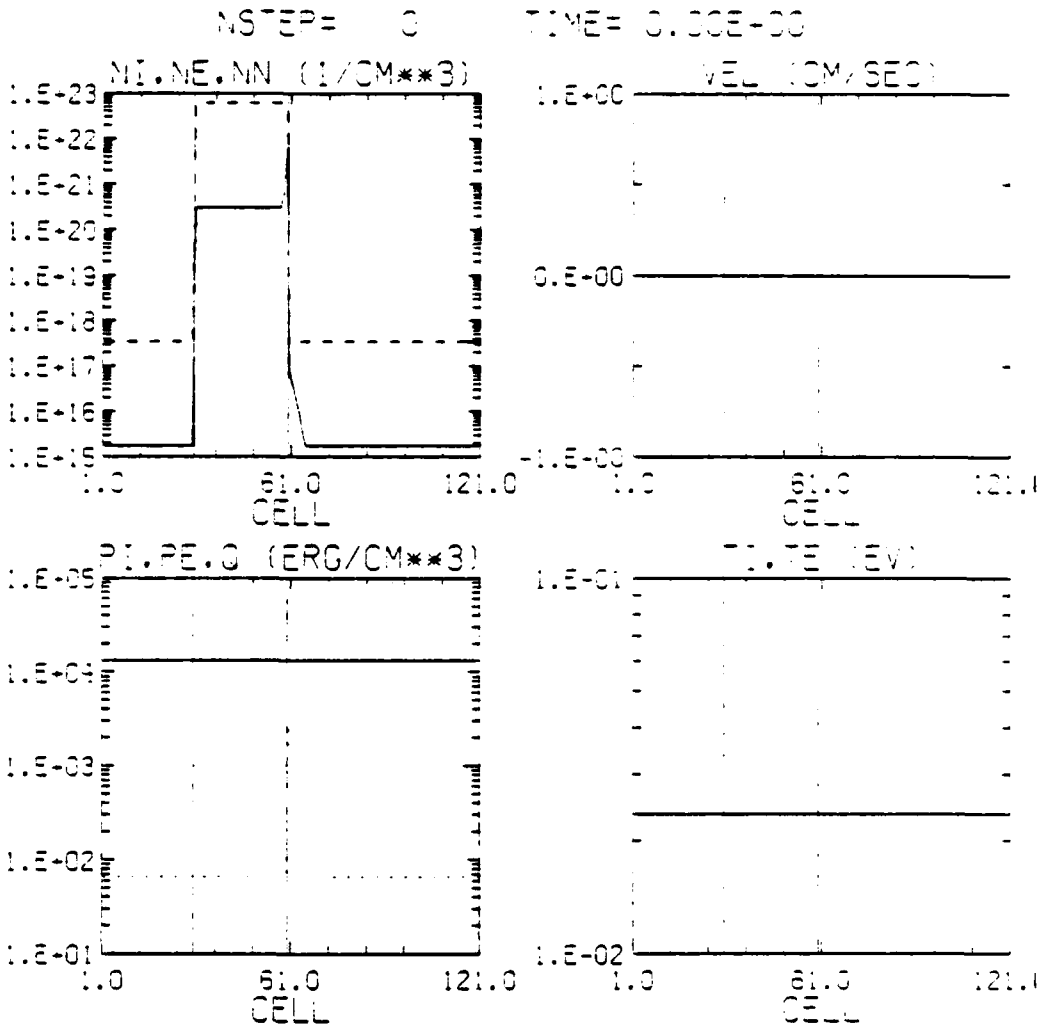

Figure 4a. Number density (NI = ions, NE = electrons, NN = neutrals), mass velocity, pressure (PI = ions, PE = electrons, Q = artificial viscosity) and temperature (TI = ions, TE = electrons) for the standard model at the initial time of the simulation. The abscissa is the cell number in the Lagrangian grid.

Throughout these and the following graphs the solid line in each box refers to the first quantity listed at the top of the box; the dotted line to the second quantity, and the dashed line to the third quantity. The straight vertical lines represent the boundaries separating the aluminum and nitrogen material. The aluminum resides between these lines.

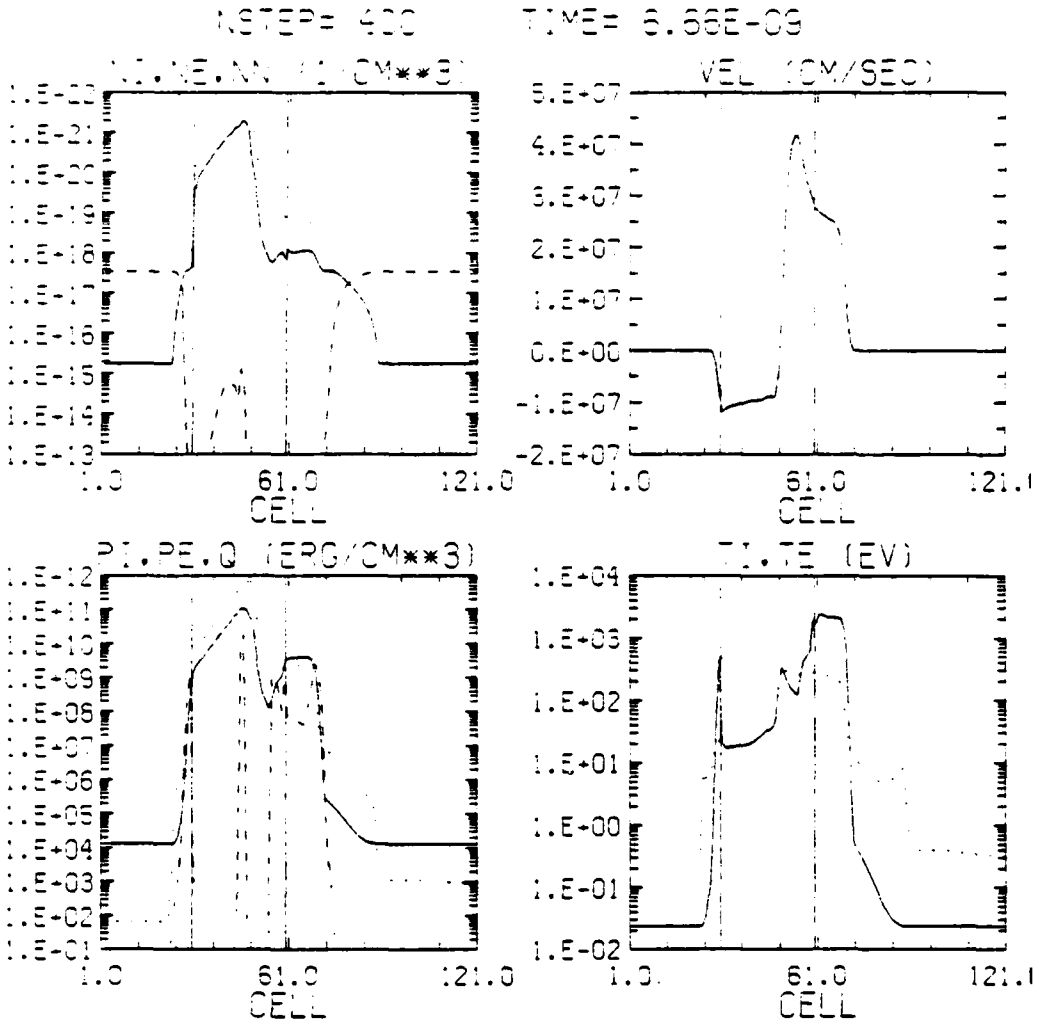

Figure 4b. Same as Fig. 4a except at 6.66 nsec after the start of the simulation.

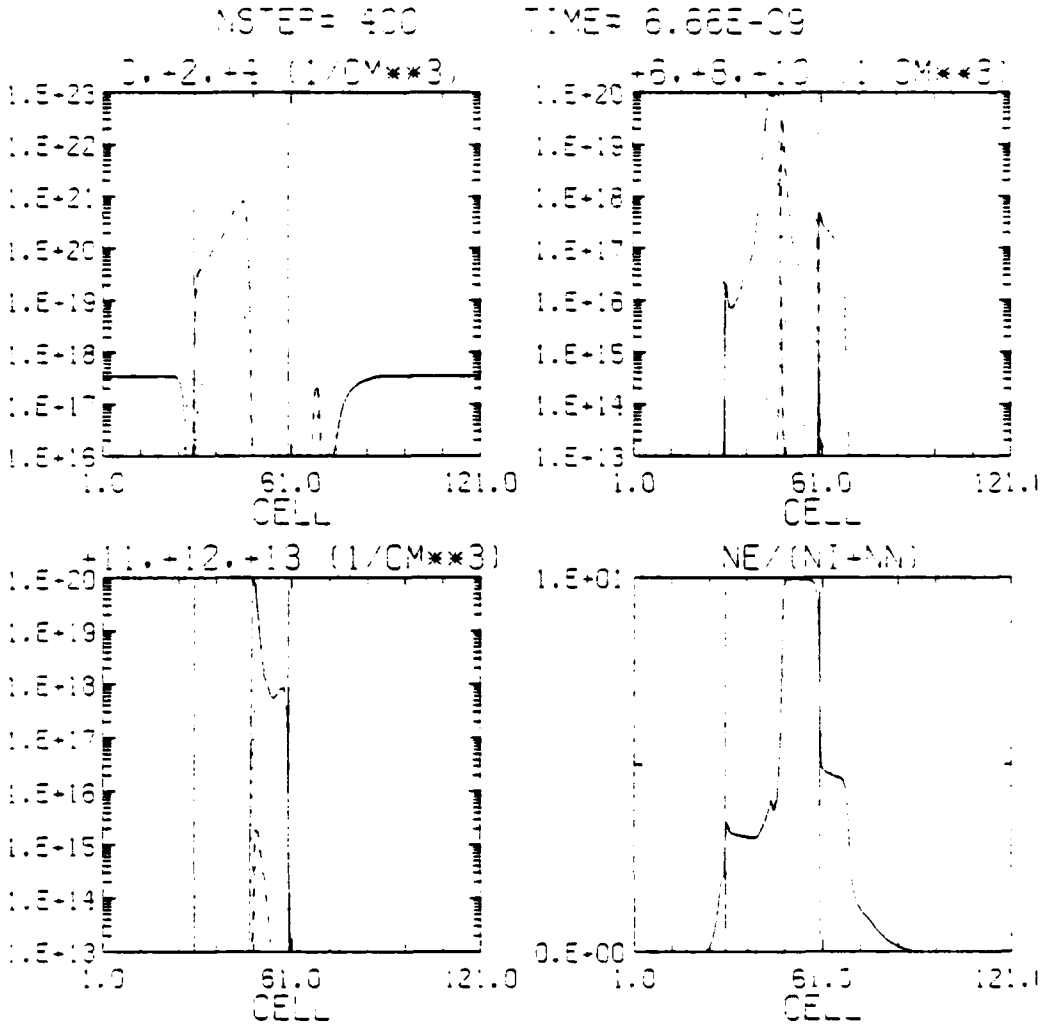

Figure 4c. The number density of different ionic species and the mean charge state at 6.66 nsec.

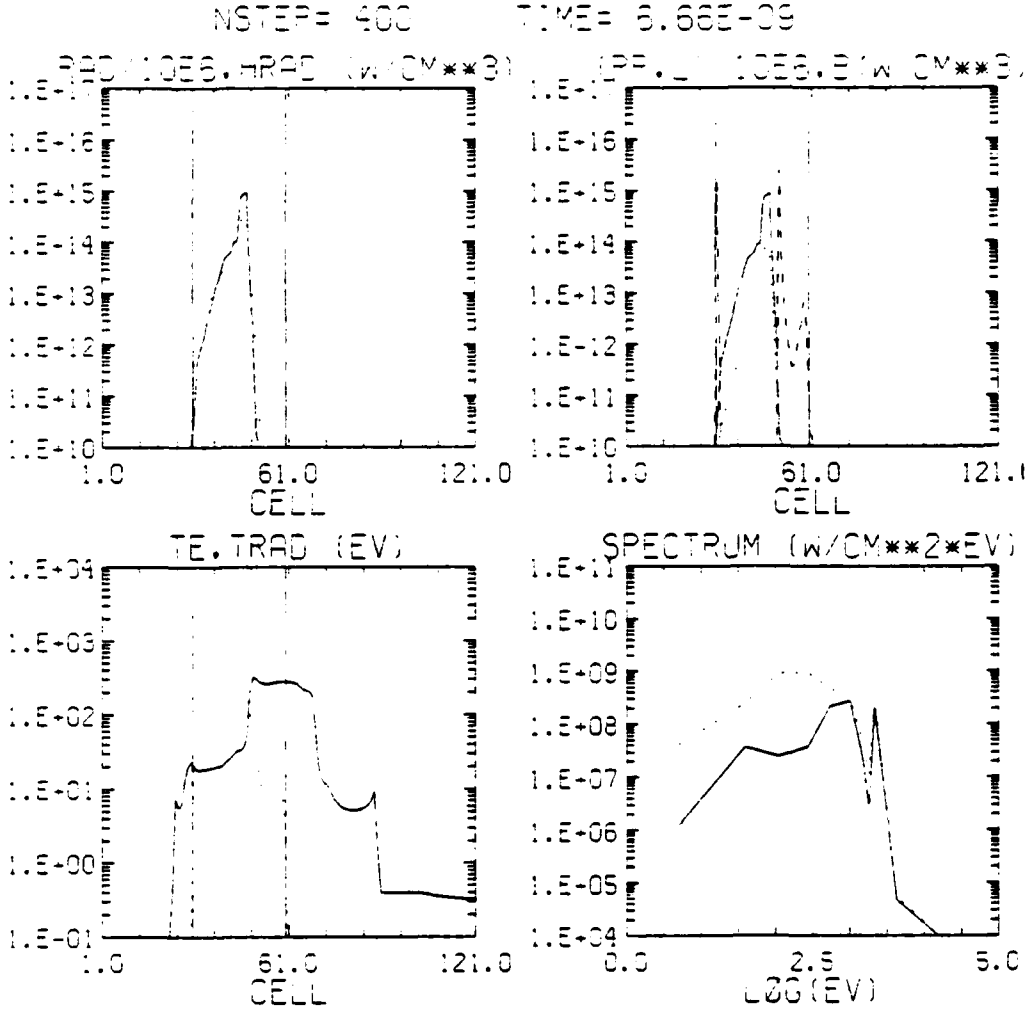

Figure 4d. The top left box shows the rate of emitted radiation per unit volume (RAD divided by 1×10^6) and the rate of heating per unit volume (HRAD) due to absorption of the radiation. The top right box breaks down the emitted radiation into recombination (RR), line (L), and bremstrahlung (B). The bottom left box shows the electron temperature (TE) and an effective radiation temperature (TRAD) based on a blackbody flux. The bottom right box shows the smoothed spectrum emerging from the back side (solid line) and front side (dotted line). The simulation time of 6.66 nsec is shortly after the peak intensity of the laser pulse (5 nsec).

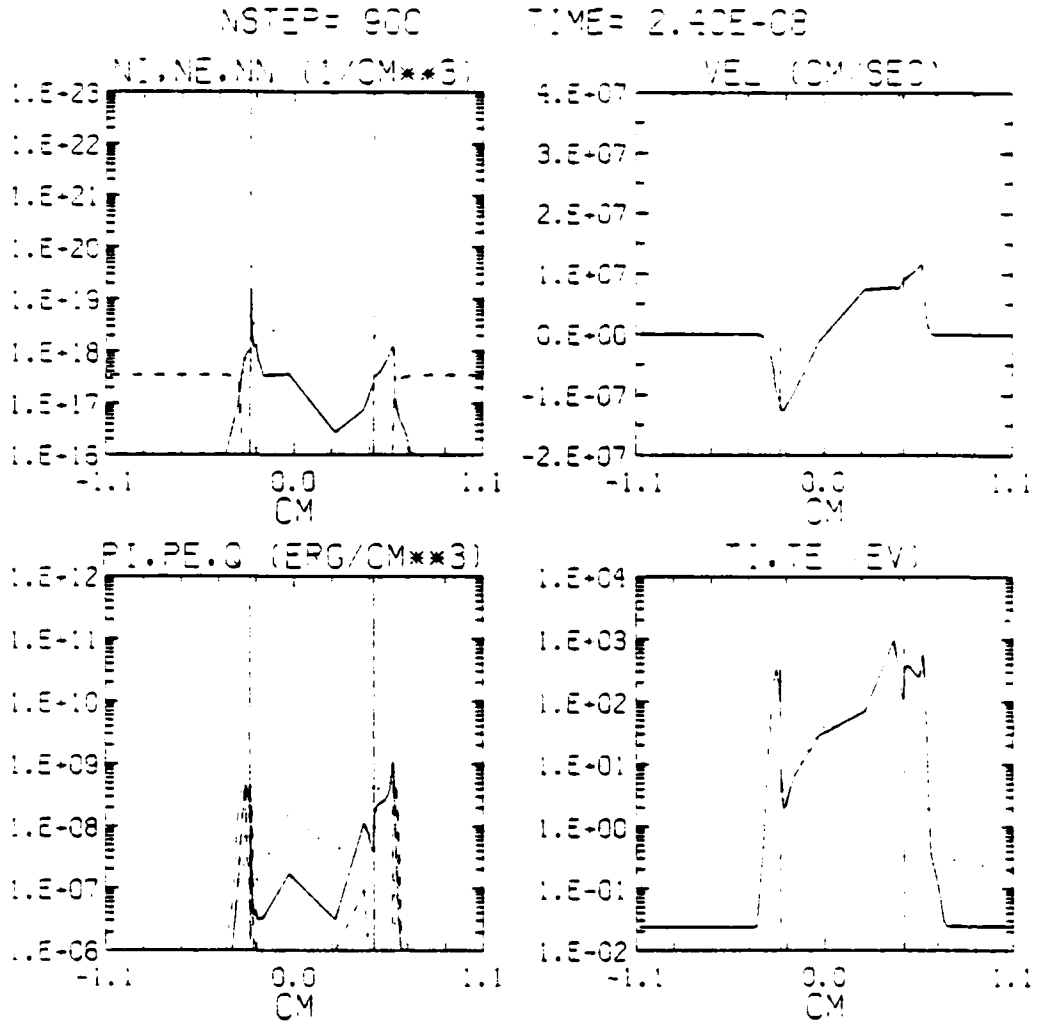

Figure 4e. Number density (NI = ions, NE = electrons, NN = neutrals), mass velocity, pressure (PI = ions, PE = electrons, Q = artificial viscosity) and temperature (TI = ions, TE = electrons) for the standard model at the simulation time 24.0 nsec. The abscissa here and in the following graphs is in physical dimensions.

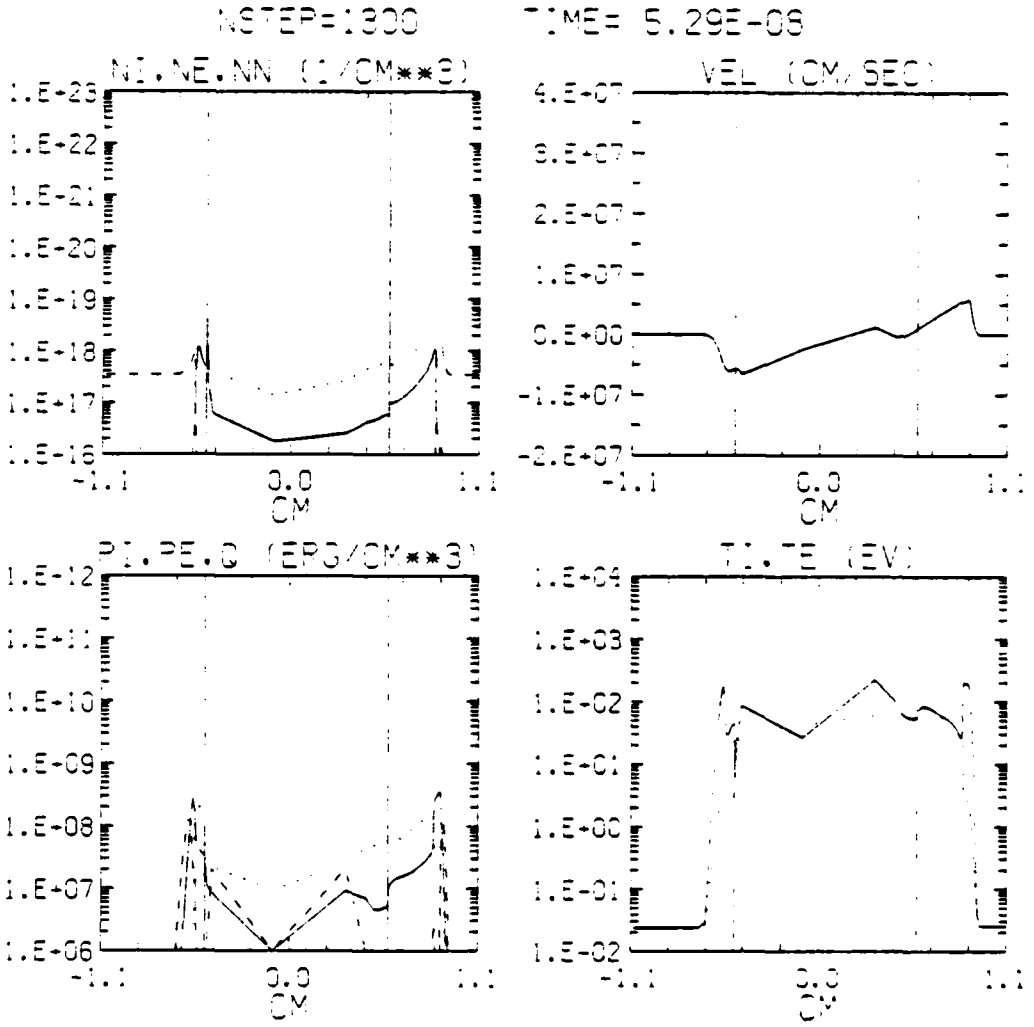

Figure 4f. Same as Fig. 4e except at the simulation time 52.9 nsec.

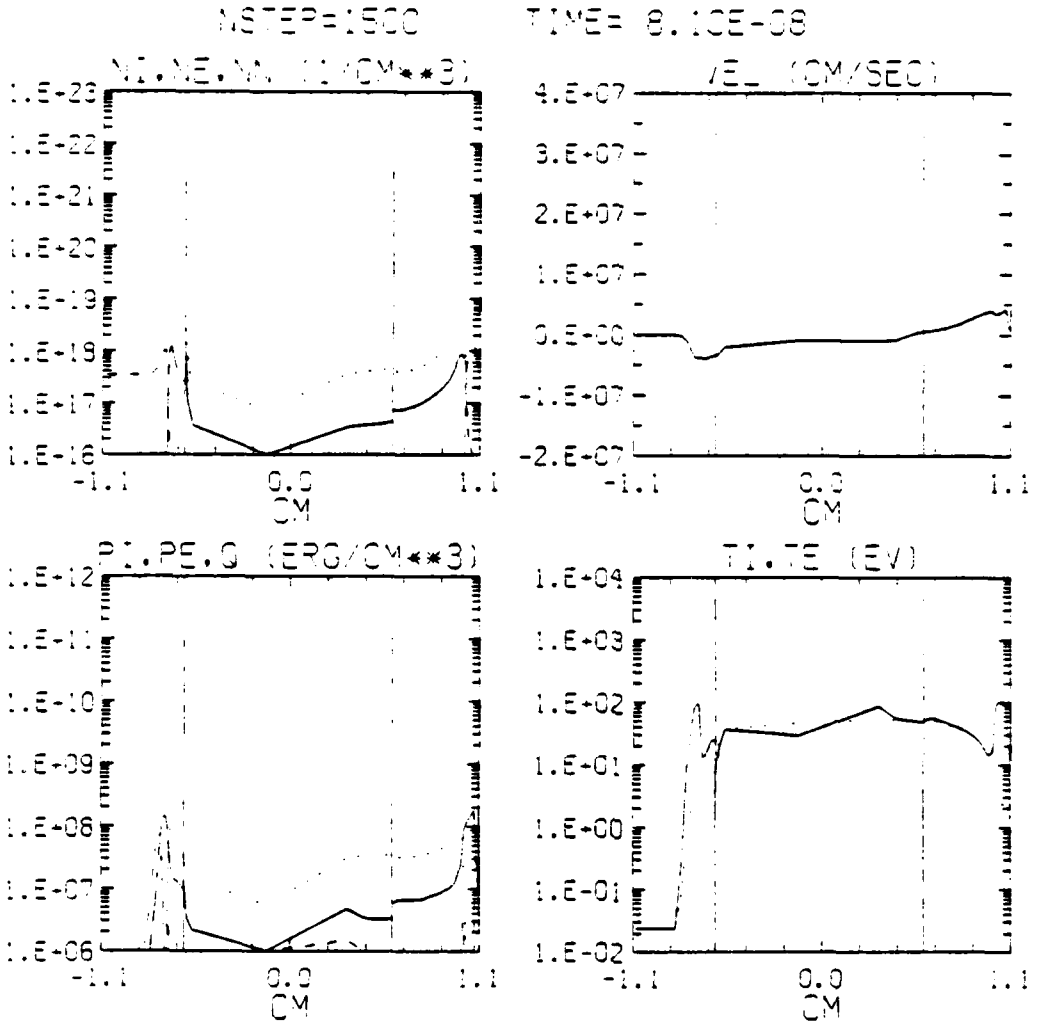

Figure 4g. Same as Fig. 4e except at the simulation time 81.0 nsec.

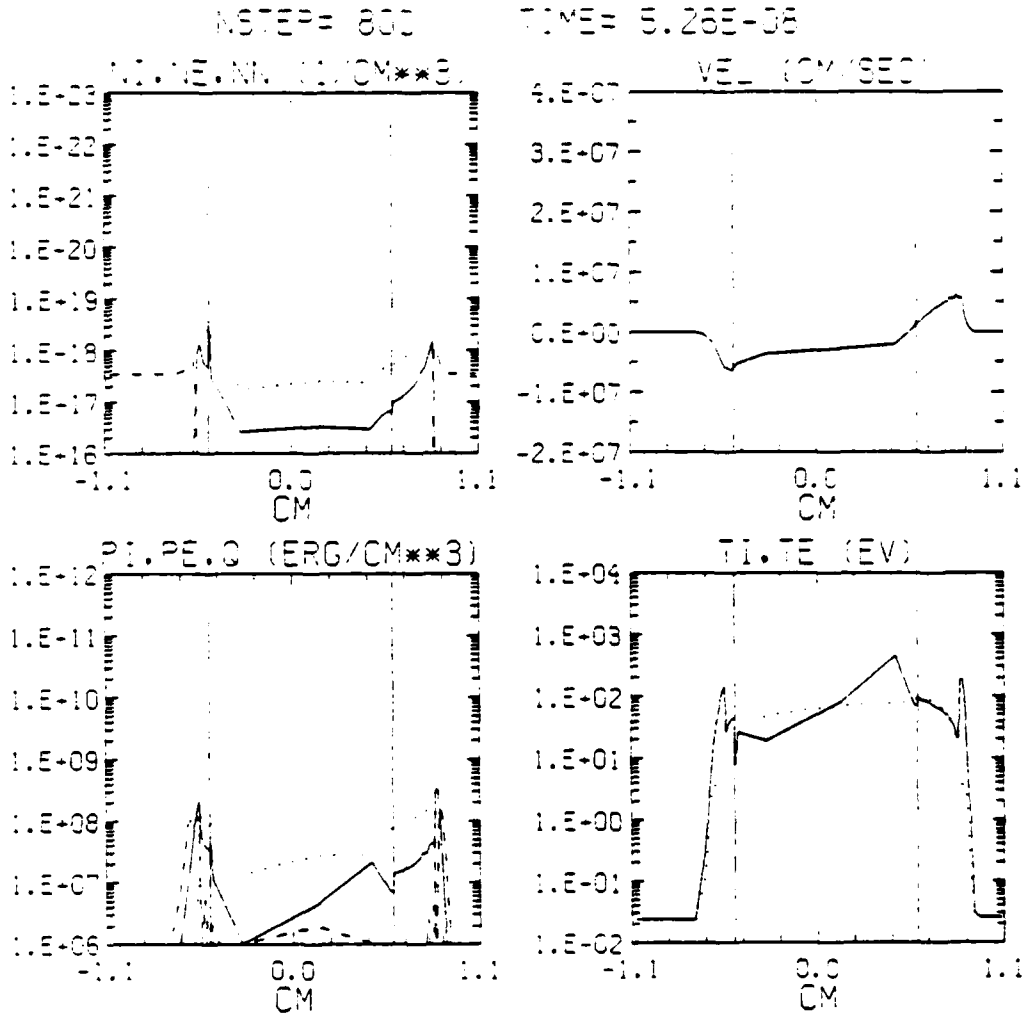

Figure 5a. Number density (NI = ions, NE = electrons, NN = neutrals), mass velocity, pressure (PI = ions, PE = electrons, Q = artificial viscosity) and temperature (TI = ions, TE = electrons) for model B at the simulation time 52.6 nsec.

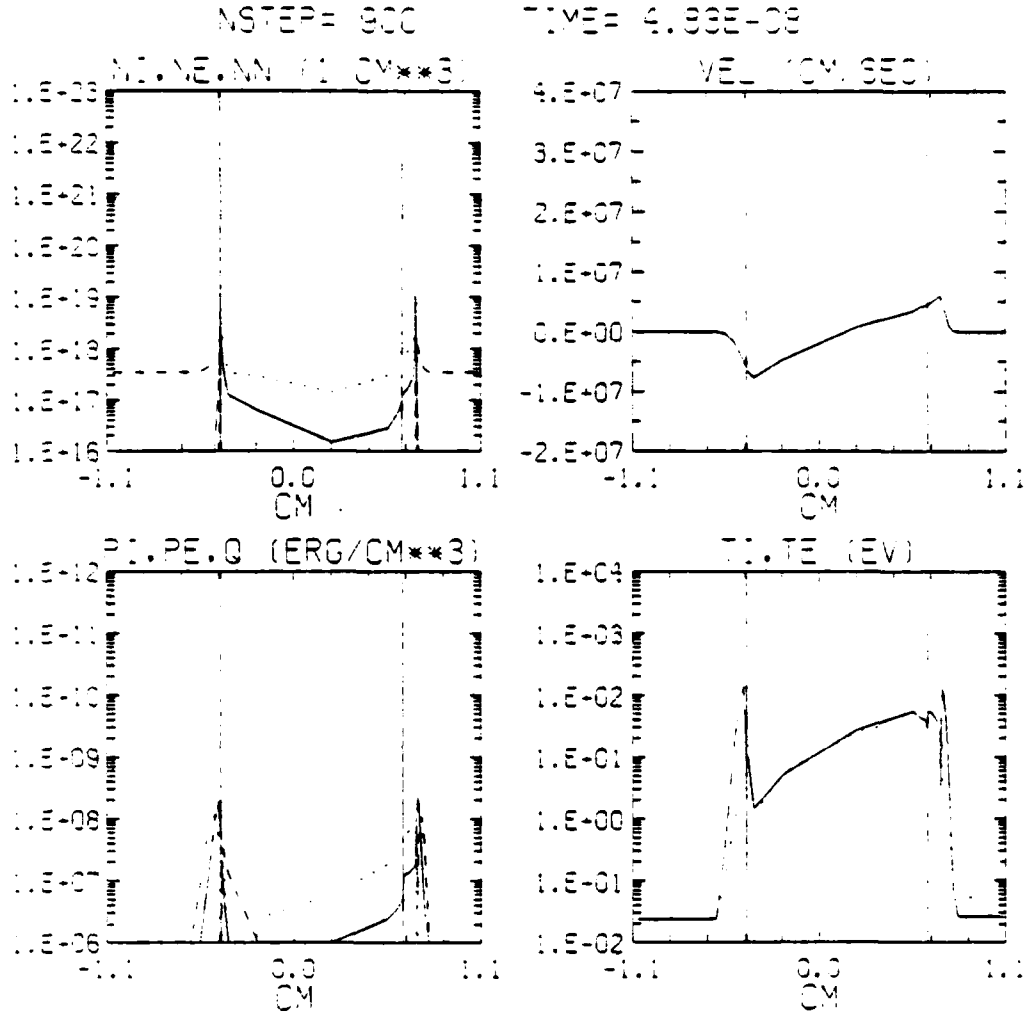

Figure 5b. Same as Fig. 5a except for model C at the simulation time 48.3 nsec.

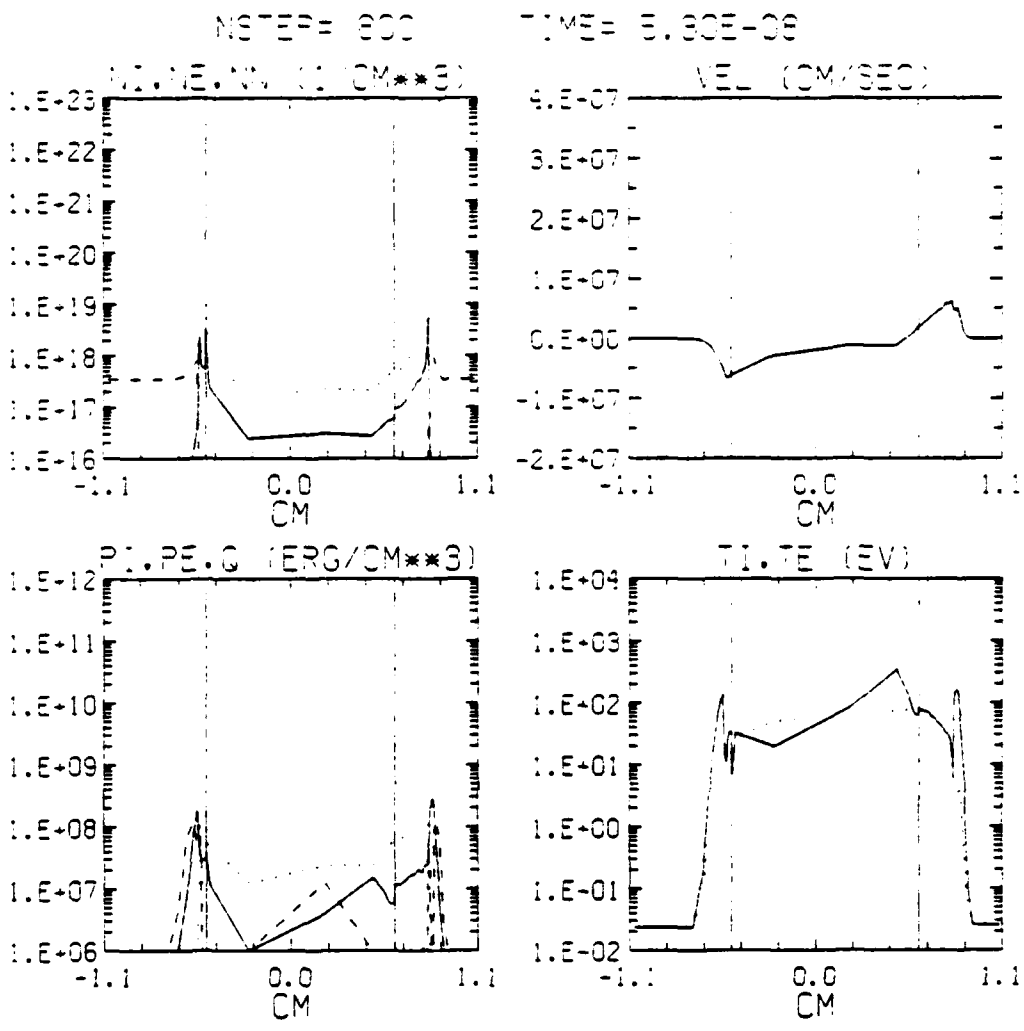

Figure 5c. Same as Fig. 5a except for model D at the simulation time 53.0 nsec.

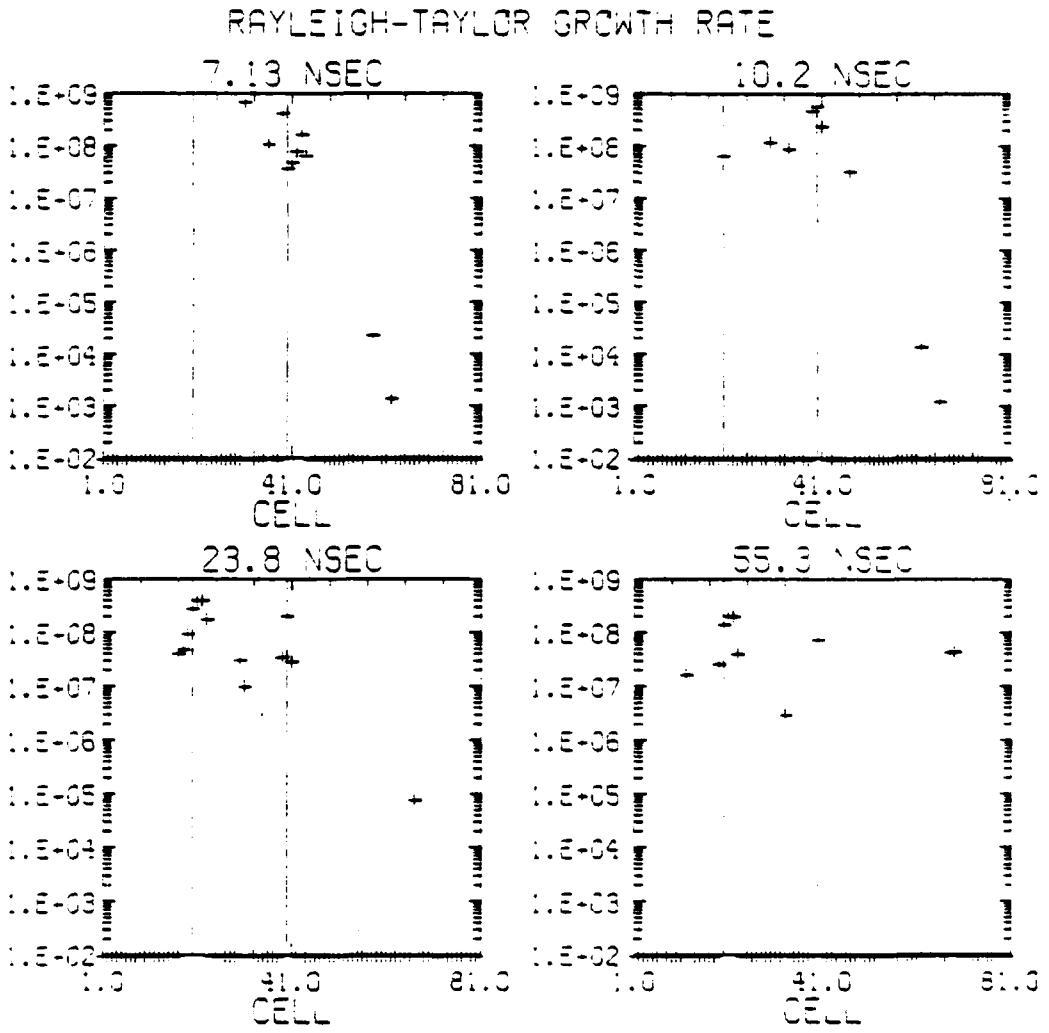

Figure 6. Growth rate in $nsec^{-1}$ for the deceleration Rayleigh-Taylor instability at four times for the standard model. The rates are calculated from eqn.(32) of the text.

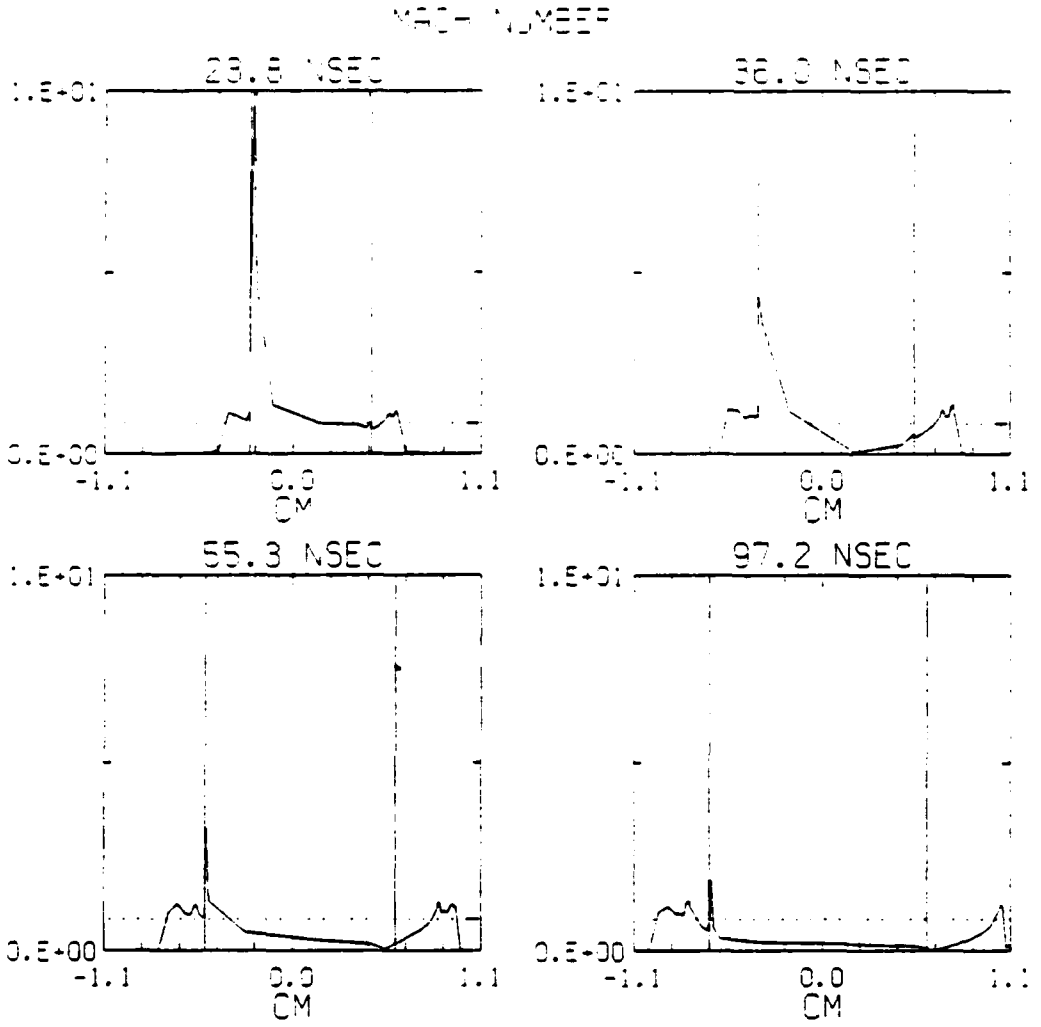

Figure 7. The local adiabatic ($\gamma = 5/3$) Mach number as a function of position for four different times in the standard model. The horizontal dashed line is at the value unity.

REFERENCES

1. B. H. Ripin, J. Grun, S. Kacenjar, E. A. McLean, and J. A. Stamper, NRL Memo Report #5268, "Introduction to the Laser-Hane Experiment and Summary of Low Pressure Interaction Results," (1984). (AD-A138 945)
2. J. A. Stamper, B. H. Ripin, and S. P. Oberschain, NRL Memo Report #5278, "Optical Imaging of a Coupling Region Between Interstreaming Plasma," (1984). (AD-A139 191)
3. B. H. Ripin, J. A. Stamper, and E. A. McLean, NRL Memo Report #5279, "Blast Wave Analysis of High Pressure Coupling Shells," (1984). (1984). (AD-A139 687)
4. S. I. Braginskii, "Transport Processes in A Plasma", in Reviews of Plasma Physics, Vol. I, ed. M. A. Leontovich, (Consultants Bureau: New York, 1965), p.205.
5. W. F. Noh, "Artificial Viscosity(Q) and Artificial Heat Flux(H) Errors for Spherically Divergent Shocks", Lawrence Livermore National Laboratory, Livermore, CA, UCRL-89623 (1983).
6. K. Hain, NRL Memo Report #3954, "ARIS Manual", (1979). (AD-A067 830)
7. R. F. Stellingwerf, DNA-TR-84-174, "Laser Target Design Scaling for the Upgraded NRL Facility", (1984). (AD-A156 030)
8. G. Arfken, Mathematical Methods for Physicists, (Academic Press: New York), p. 107.
9. R. C. Malone, R. L. McCrory, and R. L. Morse, Phys. Rev. Letters, 34, 721, (1975).
10. L. Spitzer, Jr. Physics of Fully Ionized Gases, (Interscience: New York, 1963), p.143.

11. W. M. Manheimer, Phys. of Fluids, 20, 265, "Energy Flux Limitation by Ion Acoustic Turbulence in Laser Fusion Schemes", (1977).

12. D. F. Smith and C. G. Lilliequist, Astophys. J., 232, 582, "Confinement of Hot, Hard X-Ray Producing Electrons in Solar Flares", (1979).

13. J. F. Luciani, P. Mora, and J. Virmont, Phys. Rev. Letters, 51, 1664, "Nonlocal Heat Transport Due to Steep Temperature Gradients", (1983).

14. S. L. Thompson and H. S. Lauson, Sandia Laboratories Report SC-RR-71 0714, "Improvements in the Chart D Radiation-Hydrodynamic Code III: Revised Analytic Equations of State", (1979).

15. R. F. Schmalz and J. Meyer-ter-Vehn, Phys. of Fluids, 28, 932, "Equation of State Effects on Laser Accelerated Foils", (1985).

16. D. Duston, R. W. Clark, J. Davis, and J. P. Apruzese, Phys. Rev. A., 27, 1441, "Radiation Energetics of a Laser-Produced Plasma", (1983).

17. E. Hyman, M. Mulbrandon, and J. D. Huba, NRL Memo Report #5146, "Preliminary Report on UVDEP and PRODEP Results for the Laser/HANE Experiment", (1983). (AD-A132 110)

18. J. Stamper, B. H. Ripin, E. A. McLean, C. K. Manka, and A. N. Mostovych, reported at the "Early-Time High-Altitude Working Group Meeting", held at NRL, November, 1984.

19. J. Stamper, reported at the "Early-Time High-Altitude Working Group Meeting", held at NRL, May, 1985.

20. A. Solinger, S. Rappaport, and J. Buff, Astrophys. J., 201, 381, "Isothermal Blast Wave Model of Supernova Remnants," (1975).

21. J. L. Giuliani, NRL Memo Report #5671, "Obstacles as Probes of the Blast Wave Interior in the NRL Laser/HANE Simulation Experiment", 1985. (AD-A162 535)

22. R. F. Stellingwerf, C. L. Longmire, and R. E. Peterkin, AMRC-R-700, "Models of Early Time Hane Phenomena", (1985).

23. C. K. Manka and E. A. McLean, reported at the "Early-Time High-Altitude Working Group Meeting," held at NRL, May, 1985.

24. C. Jordan, Monthly Notices Royal Astro. Soc., 142, 501, "The Ionization Equilibrium of Elements between Carbon and Nickel", (1969).

25. D. G. Colombant, K. G. Whitney, D. A. Tidman, N. K. Winsor, J. Davis, Phys. Fluids, 18, 1687, "Laser Target Model", (1975).

26. J. U. Brackbill and S. R. Goldman, Comm. Pure and Applied Math, 36, 415, "Magnetohydrodynamics in Laser Fusion: Fluid Modeling of Energy Transport in Laser Targets", (1983).

27. G. J. Pert, J. Comp. Phys., 43, 111, "Algorithms for the Self-Consistent Generation of Magnetic Fields in Plasmas", (1981).

DISTRIBUTION LIST

DEPARTMENT OF DEFENSE

ASSISTANT SECRETARY OF DEFENSE
COMM, CMD, CONT 7 INTELL
WASHINGTON, DC 20301

DIRECTOR
COMMAND CONTROL TECHNICAL CENTER
PENTAGON RM BE 685
WASHINGTON, DC 20301
01CY ATTN C-650
01CY ATTN C-312 R. MASON

DIRECTOR
DEFENSE ADVANCED RSCH PROJ AGENCY
ARCHITECT BUILDING
1400 WILSON BLVD.
ARLINGTON, VA 22209
01CY ATTN NUCLEAR MONITORING RESEARCH
01CY ATTN STRATEGIC TECH OFFICE

DEFENSE COMMUNICATION ENGINEER CENTER
1860 WIEHLE AVENUE
RESTON, VA 22090
01CY ATTN CODE R410
01CY ATTN CODE R812

DIRECTOR
DEFENSE NUCLEAR AGENCY
WASHINGTON, DC 20305
01CY ATTN STVL
04CY ATTN TITL
01CY ATTN DDST
03CY ATTN RAAE

COMMANDER
FIELD COMMAND
DEFENSE NUCLEAR AGENCY
KIRTLAND, AFB, NM 87115
01CY ATTN FCPR

DEFENSE NUCLEAR AGENCY
SAO/DNA
BUILDING 20676
KIRTLAND AFB, NM 87115
01CY D.C. THORNBURG

DIRECTOR
INTERSERVICE NUCLEAR WEAPONS SCHOOL
KIRTLAND AFB, NM 87115
01CY ATTN DOCUMENT CONTROL

JOINT PROGRAM MANAGEMENT OFFICE
WASHINGTON, DC 20330
01CY ATTN J-3 WWMCCS EVALUATION OFFICE

DIRECTOR
JOINT STRAT TGT PLANNING STAFF
OFFUTT AFB
OMAHA, NB 68113
01CY ATTN JSTPS/JLKS
01CY ATTN JPST G. GOETZ

CHIEF
LIVERMORE DIVISION FLD COMMAND DNA
DEPARTMENT OF DEFENSE
LAWRENCE LIVERMORE LABORATORY
P.O. BOX 808
LIVERMORE, CA 94550
01CY ATTN FCPRL

COMMANDANT
NATO SCHOOL (SHAPE)
APO NEW YORK 09172
01CY ATTN U.S. DOCUMENTS OFFICER

UNDER SECY OF DEF FOR RSCH & ENGRG
DEPARTMENT OF DEFENSE
WASHINGTON, DC 20301
01CY ATTN STRATEGIC & SPACE SYSTEMS (OS)

COMMANDER/DIRECTOR
ATMOSPHERIC SCIENCES LABORATORY
U.S. ARMY ELECTRONICS COMMAND
WHITE SANDS MISSILE RANGE, NM 88002
01CY ATTN DELAS-EC, F. NILES

DIRECTOR
BMD ADVANCED TECH CTR
HUNTSVILLE OFFICE
P.O. BOX 1500
HUNTSVILLE, AL 35807
01CY ATTN ATC-T MELVIN T. CAPPS
01CY ATTN ATC-O W. DAVIES
01CY ATTN ATC-R DON RUSS

PROGRAM MANAGER
BMD PROGRAM OFFICE
5001 EISENHOWER AVENUE
ALEXANDRIA, VA 22333
01CY ATTN DACS-BMT J. SHEA

CHIEF C-E- SERVICES DIVISION
U.S. ARMY COMMUNICATIONS CMD
PENTAGON RM 1B269
WASHINGTON, DC 20310
01CY ATTN C- E-SERVICES DIVISION

COMMANDER
FRADCOM TECHNICAL SUPPORT ACTIVITY
DEPARTMENT OF THE ARMY
FORT MONMOUTH, N.J. 07703
01CY ATTN DRSEL-NL-RD H. BENNET
01CY ATTN DRSEL-PL-ENV H. BOMKE
01CY ATTN J.E. QUIGLEY

COMMANDER
U.S. ARMY COMM-ELEC ENGRG INSTAL AGY
FT. HUACHUCA, AZ 85613
01CY ATTN CCC-EMEO GEORGE LANE

COMMANDER
U.S. ARMY FOREIGN SCIENCE & TECH CTR
220 7TH STREET, NE
CHARLOTTESVILLE, VA 22901
01CY ATTN DRXST-SD

COMMANDER
U.S. ARMY MATERIAL DEV & READINESS CMD
5001 EISENHOWER AVENUE
ALEXANDRIA, VA 22333
01CY ATTN DRCLDC J.A. BENDER

COMMANDER
U.S. ARMY NUCLEAR AND CHEMICAL AGENCY
7500 BACKLICK ROAD
BLDG 2073
SPRINGFIELD, VA 22150
01CY ATTN LIBRARY

DIRECTOR
U.S. ARMY BALLISTIC RESEARCH
LABORATORY
ABERDEEN PROVING GROUND, MD 21005
01CY ATTN TECH LIBRARY,
EDWARD BAICY

COMMANDER
U.S. ARMY SATCOM AGENCY
FT. MONMOUTH, NJ 07703
01CY ATTN DOCUMENT CONTROL

COMMANDER
U.S. ARMY MISSILE INTELLIGENCE AGENCY
REDSTONE ARSENAL, AL 35809
01CY ATTN JIM GAMBLE

DIRECTOR
U.S. ARMY TRADOC SYSTEMS ANALYSIS
ACTIVITY
WHITE SANDS MISSILE RANGE, NM 88002
01CY ATTN ATAA-SA
01CY ATTN TCC/F. PAYAN JR.
01CY ATTN ATTA-TAC LTC J. HESSE

COMMANDER
NAVAL ELECTRONIC SYSTEMS COMMAND
WASHINGTON, DC 20360
01CY ATTN NAVALEX 034 T. HUGHES
01CY ATTN PME 117
01CY ATTN PME 117-T
01CY ATTN CODE 5011

COMMANDING OFFICER
NAVAL INTELLIGENCE SUPPORT CTR
4301 SUITLAND ROAD, BLDG. 5
WASHINGTON, DC 20390
01CY ATTN MR. DUBBIN STIC 12
01CY ATTN NISC-50
01CY ATTN CODE 5404 J. GALET

COMMANDER
NAVAL OCEAN SYSTEMS CENTER
SAN DIEGO, CA 92152
01CY ATTN J. FERGUSON

NAVAL RESEARCH LABORATORY
WASHINGTON, DC 20375
01CY ATTN CODE 4700 S.L. Ossakow, 26 CYS IF UNCLASS (01CY IF CLASS)
ATTN CODE 4780 J.D. HUBA, 50 CYS IF UNCLASS, 01CY IF CLASS
01CY ATTN CODE 4701 I. VITKOVITSKY
01CY ATTN CODE 7500
01CY ATTN CODE 7550
01CY ATTN CODE 7580
01CY ATTN CODE 7551
01CY ATTN CODE 7555
01CY ATTN CODE 4730 E. MCLEAN
01CY ATTN CODE 4108
01CY ATTN CODE 4730 B. RIPIN
20CY ATTN CODE 2628

COMMANDER
NAVAL SPACE SURVEILLANCE SYSTEM
DAHLGREN, VA 22448
01CY ATTN CAPT J.H. BURTON

OFFICER-IN-CHARGE
NAVAL SURFACE WEAPONS CENTER
WHITE OAK, SILVER SPRING, MD 20910
01CY ATTN CODE F31

DIRECTOR
STRATEGIC SYSTEMS PROJECT OFFICE
DEPARTMENT OF THE NAVY
WASHINGTON, DC 20376
01CY ATTN NSP-2141
01CY ATTN NSSP-2722 FRED WIMBERLY

COMMANDER
NAVAL SURFACE WEAPONS CENTER
DAHLGREN LABORATORY
DAHLGREN, VA 22448
01CY ATTN CODE DF-14 R. BUTLER

OFFICER OF NAVAL RESEARCH
ARLINGTON, VA 22217
01CY ATTN CODE 465
01CY ATTN CODE 461
01CY ATTN CODE 402
01CY ATTN CODE 420
01CY ATTN CODE 421

COMMANDER
AEROSPACE DEFENSE COMMAND/DC
DEPARTMENT OF THE AIR FORCE
ENT AFB, CO 80912
01CY ATTN DC MR. LONG

COMMANDER
AEROSPACE DEFENSE COMMAND/XPD
DEPARTMENT OF THE AIR FORCE
ENT AFB, CO 80912
01CY ATTN XPDQQ
01CY ATTN XP

AIR FORCE GEOPHYSICS LABORATORY
HANSCOM AFB, MA 01731
01CY ATTN OPR HAROLD GARDNER
01CY ATTN LKB KENNETH S.W. CHAMPION
01CY ATTN OPR ALVA T. STAIR
01CY ATTN PHD JURGEN BUCHAU
01CY ATTN PHD JOHN P. MULLEN

AF WEAPONS LABORATORY
KIRTLAND AFT, NM 87117
01CY ATTN SUL
01CY ATTN CA ARTHUR H. GUENTHER
01CY ATTN NTYCE 1LT. G. KRAJEI

AFTAC
PATRICK AFB, FL 32925
01CY ATTN TN

AIR FORCE AVIONICS LABORATORY
WRIGHT-PATTERSON AFB, OH 45433
01CY ATTN AAD WADE HUNT
01CY ATTN AAD ALLEN JOHNSON

DEPUTY CHIEF OF STAFF
RESEARCH, DEVELOPMENT, & ACQ
DEPARTMENT OF THE AIR FORCE
WASHINGTON, DC 20330
01CY ATTN AFRDQ

HEADQUARTERS
ELECTRONIC SYSTEMS DIVISION
DEPARTMENT OF THE AIR FORCE
HANSCOM AFB, MA 01731-5000
01CY ATTN J. DEAS ESD/SCD-4

COMMANDER
FOREIGN TECHNOLOGY DIVISION, AFSC
WRIGHT-PATTERSON AFB, OH 45433
01CY ATTN NICD LIBRARY
01CY ATTN ETDP B. BALLARD

COMMANDER
ROME AIR DEVELOPMENT CENTER, AFSC
GRIFFISS AFB, NY 13441
01CY ATTN DOC LIBRARY/TSLD
01CY ATTN OCSE V. COYNE

STRATEGIC AIR COMMAND/XPFS
OFFUTT AFB, NB 68113
01CY ATTN ADWATE MAJ BRUCE BAUER
01CY ATTN NRT
01CY ATTN DOK CHIEF SCIENTIST

SAMSO/SK
P.O. BOX 92960
WORLDWAY POSTAL CENTER
LOS ANGELES, CA 90009
01CY ATTN SKA (SPACE COMM SYSTEMS)
M. CLAVIN

SAMSO/MN
NORTON AFB, CA 92409
(MINUTEMAN)
01CY ATTN MNNL

COMMANDER
ROME AIR DEVELOPMENT CENTER, AFSC
HANSCOM AFB, MA 01731
01CY ATTN EEP A. LORENTZEN

DEPARTMENT OF ENERGY
LIBRARY ROOM G-042
WASHINGTON, DC 20545
01CY ATTN DOC CON FOR A. LABOWITZ

DEPARTMENT OF ENERGY
ALBUQUERQUE OPERATIONS OFFICE
P.O. BOX 5400
ALBUQUERQUE, NM 87115
01CY ATTN DOC CON FOR D. SHERWOOD

EG&G, INC.
LOS ALAMOS DIVISION
P.O. BOX 809
LOS ALAMOS, NM 85544
01CY ATTN DOC CON FOR J. BREEDLOVE

UNIVERSITY OF CALIFORNIA
LAWRENCE LIVERMORE LABORATORY
P.O. BOX 808
LIVERMORE, CA 94550
01CY ATTN DOC CON FOR TECH INFO
DEPT
01CY ATTN DOC CON FOR L-389 R. OTT
01CY ATTN DOC CON FOR L-31 R. HAGER

LOS ALAMOS NATIONAL LABORATORY
P.O. BOX 1663
LOS ALAMOS, NM 87545
01CY ATTN DOC CON FOR J. WOLCOTT
01CY ATTN DOC CON FOR R.F. TASCHEK
01CY ATTN DOC CON FOR E. JONES
01CY ATTN DOC CON FOR J. MALIK
01CY ATTN DOC CON FOR R. JEFFRIES
01CY ATTN DOC CON FOR J. ZINN
01CY ATTN DOC CON FOR D. WESTERVELT
01CY ATTN D. SAPPENFIELD

LOS ALAMOS NATIONAL LABORATORY
MS D438
LOS ALAMOS, NM 87545
01CY ATTN S.P. GARY
01CY ATTN J. BOROVSKY

SANDIA LABORATORIES
P.O. BOX 5800
ALBUQUERQUE, NM 87115
01CY ATTN DOC CON FOR W. BROWN
01CY ATTN DOC CON FOR A.
THORNBROUGH
01CY ATTN DOC CON FOR T. WRIGHT
01CY ATTN DOC CON FOR D. DAHLGREN
01CY ATTN DOC CON FOR 3141
01CY ATTN DOC CON FOR SPACE PROJECT
DIV

SANDIA LABORATORIES
LIVERMORE LABORATORY
P.O. BOX 969
LIVERMORE, CA 94550
01CY ATTN DOC CON FOR B. MURPHEY
01CY ATTN DOC CON FOR T. COOK

OFFICE OF MILITARY APPLICATION
DEPARTMENT OF ENERGY
WASHINGTON, DC 20545
01CY ATTN DOC CON DR. YO SONG

OTHER GOVERNMENT

INSTITUTE FOR TELECOM SCIENCES
NATIONAL TELECOMMUNICATIONS & INFO
ADMIN
BOULDER, CO 80303
01CY ATTN L. BERRY

NATIONAL OCEANIC & ATMOSPHERIC ADMIN
ENVIRONMENTAL RESEARCH LABORATORIES
DEPARTMENT OF COMMERCE
BOULDER, CO 80302
01CY ATTN R. GRUBB
01CY ATTN AERONOMY LAB G. REID

DEPARTMENT OF DEFENSE CONTRACTORS

AEROSPACE CORPORATION
P.O. BOX 92957
LOS ANGELES, CA 90009
01CY ATTN I. GARFUNKEL
01CY ATTN T. SALMI
01CY ATTN V. JOSEPHSON
01CY ATTN S. BOWER
01CY ATTN D. OLSEN

ANALYTICAL SYSTEMS ENGINEERING CORP
5 OLD CONCORD ROAD
BURLINGTON, MA 01803
01CY ATTN RADIO SCIENCES

AUSTIN RESEARCH ASSOC., INC.
1901 RUTLAND DRIVE
AUSTIN, TX 78758
01CY ATTN L. SLOAN
01CY ATTN R. THOMPSON

BERKELEY RESEARCH ASSOCIATES, INC.
P.O. BOX 983
BERKELEY, CA 94701
01CY ATTN J. WORKMAN
01CY ATTN C. PRETTIE
01CY ATTN S. BRECHT

BOEING COMPANY, THE
P.O. BOX 3707
SEATTLE, WA 98124
01CY ATTN G. KEISTER
01CY ATTN D. MURRAY
01CY ATTN G. HALL
01CY ATTN J. KENNEY

CHARLES STARK DRAPER LABORATORY, INC.
555 TECHNOLOGY SQUARE
CAMBRIDGE, MA 02139
01CY ATTN D.B. COX
01CY ATTN J.P. GILMORE

COMSAT LABORATORIES
LINTHICUM ROAD
CLARKSBURG, MD 20734
01CY ATTN G. HYDE

CORNELL UNIVERSITY
DEPARTMENT OF ELECTRICAL ENGINEERING
ITHACA, NY 14850
01CY ATTN D.T. FARLEY, JR.

ELECTROSPACE SYSTEMS, INC.
BOX 1359
RICHARDSON, TX 75080
01CY ATTN H. LOGSTON
01CY ATTN SECURITY (PAUL PHILLIPS)

EOS TECHNOLOGIES, INC.
606 Wilshire Blvd.
Santa Monica, CA 90401
01CY ATTN C.B. GABBARD
01CY ATTN R. LELEVIER

ESL, INC.
495 JAVA DRIVE
SUNNYVALE, CA 94086
01CY ATTN J. ROBERTS
01CY ATTN JAMES MARSHALL

GENERAL ELECTRIC COMPANY
SPACE DIVISION
VALLEY FORGE SPACE CENTER
GODDARD BLVD KING OF PRUSSIA
P.O. BOX 8555
PHILADELPHIA, PA 19101
01CY ATTN M.H. BORTNER
SPACE SCI LAB

GENERAL ELECTRIC TECH SERVICES
CO., INC.
HMES
COURT STREET
SYRACUSE, NY 13201
01CY ATTN G. MILLMAN

GEOPHYSICAL INSTITUTE
UNIVERSITY OF ALASKA
FAIRBANKS, AK 99701
(ALL CLASS ATTN: SECURITY OFFICER)
01CY ATTN T.N. DAVIS (UNCLASS ONLY)
01CY ATTN TECHNICAL LIBRARY
01CY ATTN NEAL BROWN (UNCLASS ONLY)

GTE SYLVANIA, INC.
ELECTRONICS SYSTEMS GRP-EASTERN DIV
77 A STREET
NEEDHAM, MA 02194
01CY ATTN DICK STEINHOF

HSS, INC.
2 ALFRED CIRCLE
BEDFORD, MA 01730
01CY ATTN DONALD HANSEN

ILLINOIS, UNIVERSITY OF
107 COBLE HALL
150 DAVENPORT HOUSE
CHAMPAIGN, IL 61820
(ALL CORRES ATTN DAN MCCLELLAND)
01CY ATTN K. YEH

INSTITUTE FOR DEFENSE ANALYSES
1801 NO. BEAUREGARD STREET
ALEXANDRIA, VA 22311
01CY ATTN J.M. AEIN
01CY ATTN ERNEST BAUER
01CY ATTN HANS WOLFARD
01CY ATTN JOEL BENGSTON

INTL TEL & TELEGRAPH CORPORATION
500 WASHINGTON AVENUE
NUTLEY, NJ 07110
01CY ATTN TECHNICAL LIBRARY

JAYCOR
1011 TORREYANA ROAD
P.O. BOX 85154
SAN DIEGO, CA 92138
01CY ATTN J.L. SPERLING

JOHNS HOPKINS UNIVERSITY
APPLIED PHYSICS LABORATORY
JOHNS HOPKINS ROAD
LAUREL, MD 20810
01CY ATTN DOCUMENT LIBRARIAN
01CY ATTN THOMAS POTEMRA
01CY ATTN JOHN DASSOULAS

KAMAN SCIENCES CORP
P.O. BOX 7463
COLORADO SPRINGS, CO 80933
01CY ATTN T. MEAGHER

KAMAN TEMPO-CENTER FOR ADVANCED STUDIES
816 STATE STREET (P.O DRAWER QQ)
SANTA BARBARA, CA 93102
01CY ATTN DASIAC
01CY ATTN WARREN S. KNAPP
01CY ATTN WILLIAM MCNAMARA
01CY ATTN B. GAMBILL

LINKABIT CORP
10453 ROSELLE
SAN DIEGO, CA 92121
01CY ATTN IRWIN JACOBS

LOCKHEED MISSILES & SPACE CO., INC
P.O. BOX 504
SUNNYVALE, CA 94088
01CY ATTN DEPT 60-12
01CY ATTN D.R. CHURCHILL

LOCKHEED MISSILES & SPACE CO., INC.
3251 HANOVER STREET
PALO ALTO, CA 94304
01CY ATTN MARTIN WALT DEPT 52-12
01CY ATTN W.L. IMHOF DEPT 52-12
01CY ATTN RICHARD G. JOHNSON DEPT 52-12
01CY ATTN J.B. CLADIS DEPT 52-12

MARTIN MARIETTA CORP
ORLANDO DIVISION
P.O. BOX 5837
ORLANDO, FL 32805
01CY ATTN R. HEFFNER

MCDONNEL DOUGLAS CORPORATION
5301 BOLSA AVENUE
HUNTINGTON BEACH, CA 92647
01CY ATTN N. HARRIS
01CY ATTN J. MOULE
01CY ATTN GEORGE MROZ
01CY ATTN W. OLSON
01CY ATTN R.W. HALPRIN
01CY ATTN TECHNICAL LIBRARY SERVICES

MISSION RESEARCH CORPORATION
735 STATE STREET
SANTA BARBARA, CA 93101
01CY ATTN P. FISCHER
01CY ATTN W.F. CREVIER
01CY ATTN STEVEN L. GUTSCHE
01CY ATTN R. BOGUSCH
01CY ATTN R. HENDRICK
01CY ATTN RALPH KILB
01CY ATTN DAVE SOWLE
01CY ATTN F. FAJEN
01CY ATTN M. SCHEIBE
01CY ATTN CONRAD L. LONGMIRE
01CY ATTN B. WHITE
01CY ATTN R. STAGAT

MISSION RESEARCH CORP.
1720 RANDOLPH ROAD, S.E.
ALBUQUERQUE, NM 87106
01CY R. STELLINGWERF
01CY M. ALME
01CY L. WRIGHT

MITRE CORP
WESTGATE RESEARCH PARK
1820 DOLLY MADISON BLVD
MCLEAN, VA 22101
01CY ATTN W. HALL
01CY ATTN W. FOSTER

PACIFIC-SIERRA RESEARCH CORP
12340 SANTA MONICA BLVD.
LOS ANGELES, CA 90025
01CY ATTN E.C. FIELD, JR.

PENNSYLVANIA STATE UNIVERSITY
IONOSPHERE RESEARCH LAB
318 ELECTRICAL ENGINEERING EAST
UNIVERSITY PARK, PA 16802
(NO CLASS TO THIS ADDRESS)
01CY ATTN IONOSPHERIC RESEARCH LAB

PHOTOMETRICS, INC.
4 ARROW DRIVE
WOBURN, MA 01801
01CY ATTN IRVING L. KOFSKY

PHYSICAL DYNAMICS, INC.
P.O. BOX 3027
BELLEVUE, WA 98009
01CY ATTN E.J. FREMOUW

PHYSICAL DYNAMICS, INC.
P.O. BOX 10367
OAKLAND, CA 94610
ATTN A. THOMSON

R & D ASSOCIATES
P.O. BOX 9695
MARINA DEL REY, CA 90291
01CY ATTN FORREST GILMORE
01CY ATTN WILLIAM B. WRIGHT, JR.
01CY ATTN WILLIAM J. KARZAS
01CY ATTN H. ORY
01CY ATTN C. MACDONALD

RAND CORPORATION, THE
15450 COHASSET STREET
VAN NUYS, CA 91406
01CY ATTN CULLEN CRAIN
01CY ATTN ED BEDROZIAN

RAYTHEON CO.
528 BOSTON POST ROAD
SUDBURY, MA 01776
01CY ATTN BARBARA ADAMS

RIVERSIDE RESEARCH INSTITUTE
330 WEST 42nd STREET
NEW YORK, NY 10036
01CY ATTN VINCE TRAPANI

SCIENCE APPLICATIONS, INC.
1150 PROSPECT PLAZA
LA JOLLA, CA 92037
01CY ATTN LEWIS M. LINSON
01CY ATTN DANIEL A. HAMLIN
01CY ATTN E. FRIEMAN
01CY ATTN E.A. STRAKER
01CY ATTN CURTIS A. SMITH

SCIENCE APPLICATIONS, INC
1710 GOODRIDGE DR.
MCLEAN, VA 22102
01CY J. COCKAYNE
01CY E. HYMAN

SRI INTERNATIONAL
333 RAVENSWOOD AVENUE
MENLO PARK, CA 94025
01CY ATTN J. CASPER
01CY ATTN DONALD NEILSON
01CY ATTN ALAN BURNS
01CY ATTN G. SMITH
01CY ATTN R. TSUNODA
01CY ATTN DAVID A. JOHNSON
01CY ATTN WALTER G. CHESNUT
01CY ATTN CHARLES L. RINO
01CY ATTN WALTER JAYE
01CY ATTN J. VICKREY
01CY ATTN RAY L. LEADABRAND
01CY ATTN G. CARPENTER
01CY ATTN G. PRICE
01CY ATTN R. LIVINGSTON
01CY ATTN V. GONZALES
01CY ATTN D. MCDANIEL

TECHNOLOGY INTERNATIONAL CORP
75 WIGGINS AVENUE
BEDFORD, MA 01730
01CY ATTN W.P. BOQUIST

TRW DEFENSE & SPACE SYS GROUP
ONE SPACE PARK
REDONDO BEACH, CA 90278
01CY ATTN R. K. PLEBUCH
01CY ATTN S. ALTSCHULER
01CY ATTN D. DEE
01CY ATTN D/ STOCKWELL
SNTF/1575

VISIDYNE
SOUTH BEDFORD STREET
BURLINGTON, MA 01803
01CY ATTN W. REIDY
01CY ATTN J. CARPENTER
01CY ATTN C. HUMPHREY

UNIVERSITY OF PITTSBURGH
PITTSBURGH, PA 15213
01CY ATTN: N. ZABUSKY

DIRECTOR OF RESEARCH
U. S. NAVAL ACADEMY
ANNAPOLIS, MD 21402
02CY

CODE 1220
01CY

END

FILMED

6-86

DTIC